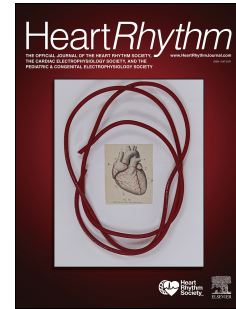


# Journal Pre-proof



Cardiac stereotactic body radiotherapy to treat malignant ventricular arrhythmias directly affects the cardiomyocyte electrophysiology

Christine Mages, MD, Heike Gampp, Ann-Kathrin Rahm, MD, Juline Hackbarth, Julia Pfeiffer, Finn Petersenn, Xenia Kramp, Fatemeh Kermani, Juan Zhang, PhD, Daniel A. Pijnappels, PhD, Antoine A.F. de Vries, PhD, Katharina Seidensaal, MD, Bernhard Rhein, PhD, Jürgen Debus, MD, Nina D. Ullrich, PhD, Norbert Frey, MD, Dierk Thomas, MD, Patrick Lugenbiel, MD

PII: S1547-5271(24)02817-0

DOI: <https://doi.org/10.1016/j.hrthm.2024.06.043>

Reference: HRTHM 10579

To appear in: *Heart Rhythm*

Received Date: 19 May 2024

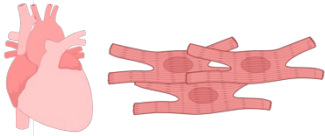
Revised Date: 21 June 2024

Accepted Date: 22 June 2024

Please cite this article as: Mages C, Gampp H, Rahm A-K, Hackbarth J, Pfeiffer J, Petersenn F, Kramp X, Kermani F, Zhang J, Pijnappels DA, de Vries AAF, Seidensaal K, Rhein B, Debus J, Ullrich ND, Frey N, Thomas D, Lugenbiel P, Cardiac stereotactic body radiotherapy to treat malignant ventricular arrhythmias directly affects the cardiomyocyte electrophysiology, *Heart Rhythm* (2024), doi: <https://doi.org/10.1016/j.hrthm.2024.06.043>.

This is a PDF file of an article that has undergone enhancements after acceptance, such as the addition of a cover page and metadata, and formatting for readability, but it is not yet the definitive version of record. This version will undergo additional copyediting, typesetting and review before it is published in its final form, but we are providing this version to give early visibility of the article. Please note that, during the production process, errors may be discovered which could affect the content, and all legal disclaimers that apply to the journal pertain.

© 2024 Published by Elsevier Inc. on behalf of Heart Rhythm Society.

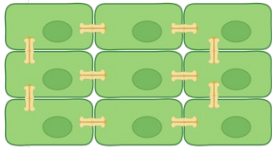
Neonatal Rat Ventricular  
CardiomyocytesIrradiation  
20 Gy Photon RadiationTime Intervals of  
Analysis

24h

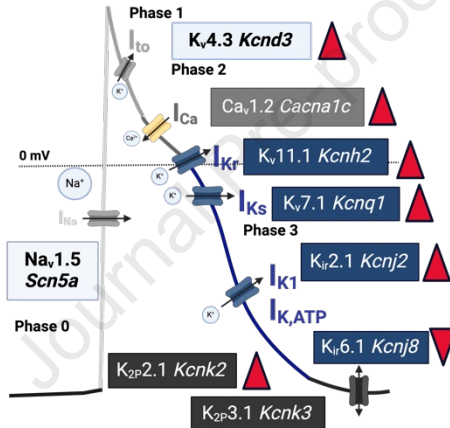
96h

Overview 96h after Irradiation

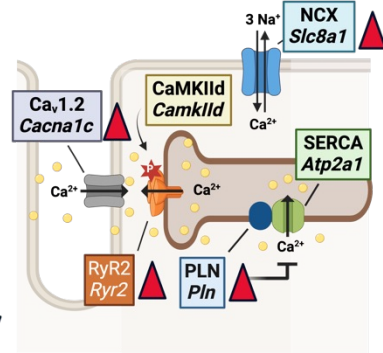
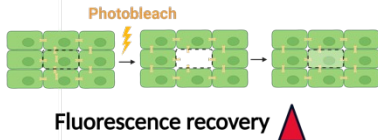
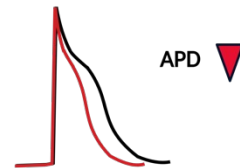
Connexin 43



Action Potential



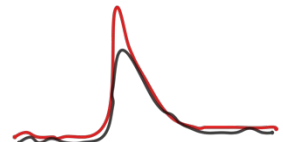
Calcium Handling

Functional Gap Junction  
AssessmentOptical Voltage Mapping and Video  
Analysis

Beating frequency

Conduction velocity

Calcium Imaging



Calcium amplitude

Decay rate

1 **Cardiac stereotactic body radiotherapy to treat malignant ventricular**  
2 **arrhythmias directly affects the cardiomyocyte electrophysiology**

3

4 **Running Title:** Cardiac SBRT Directly Modulates Cardiomyocyte Electrophysiology

5

6 **Authors:** Christine Mages, MD <sup>a,b,c,d,#</sup>, Heike Gamp <sup>a,b,#</sup>, Ann-Kathrin Rahm, MD <sup>a,b,c,d</sup>,  
7 Juline Hackbarth <sup>a,b</sup>, Julia Pfeiffer <sup>a,b</sup>, Finn Petersenn <sup>a,b</sup>, Xenia Kramp <sup>a,b</sup>, Fatemeh  
8 Kermani <sup>e</sup>, Juan Zhang, PhD <sup>f</sup>, Daniel A. Pijnappels, PhD <sup>f</sup>, Antoine A. F de Vries, PhD <sup>f</sup>,  
9 Katharina Seidensaal, MD <sup>g,h</sup>, Bernhard Rhein, PhD <sup>g,h</sup>, Jürgen Debus, MD <sup>g,h</sup>, Nina  
10 D. Ullrich, PhD <sup>c,e,i</sup>, Norbert Frey, MD <sup>a,b,c,d</sup>, Dierk Thomas, MD <sup>a,b,c</sup>, Patrick Lugenbiel,  
11 MD <sup>a,b,c\*</sup>

12

13 **Total Word Count: 5041**

14 <sup>a</sup>Department of Cardiology, University Hospital Heidelberg, Heidelberg, Germany;

15 <sup>b</sup>Heidelberg Center for Heart Rhythm Disorders (HCR), University Hospital  
16 Heidelberg, Heidelberg, Germany;

17 <sup>c</sup>German Centre for Cardiovascular Research (DZHK), Partner site  
18 Heidelberg/Mannheim, University of Heidelberg, Heidelberg, Germany;

19 <sup>d</sup>Informatics4Life Consortium (Institute for Informatics Heidelberg), Heidelberg,  
20 Germany;

21 <sup>e</sup>Division of Cardiovascular Physiology, Institute of Physiology and Pathophysiology,  
22 Heidelberg, Germany;

23 <sup>f</sup>Department of Cardiology, Leiden University Medical Center, Leiden, the Netherlands

24 <sup>g</sup>Department of Radiation Oncology, Heidelberg University Hospital, Heidelberg,  
25 Germany;

26 <sup>h</sup>Heidelberg Institute of Radiation Oncology (HIRO), Heidelberg, Germany;

27 <sup>i</sup>Department of Physiology, University of Bern, Switzerland

28

29 # authors contributed equally

30

31 **\*Address for correspondence:** Patrick Lugenbiel, MD, FEHRA; Department of  
32 Cardiology, Heidelberg University, Im Neuenheimer Feld 410, 69120 Heidelberg,  
33 Germany; E-Mail: [patrick.lugenbiel@med.uni-heidelberg.de](mailto:patrick.lugenbiel@med.uni-heidelberg.de)

34

35 **Funding:** This work was supported in part by research grants from the University of  
36 Heidelberg, Faculty of Medicine (Postdoctoral Fellowships to P.L. and A.K.R.), from  
37 the German Cardiac Society (Fellowships to A.K.R. and P.L., Otto-Hess-  
38 Promotionsstipendium to H.G.), from the Elisabeth und Rudolf-Hirsch Stiftung für  
39 Medizinische Forschung (to A.K.R), from the Ernst und Berta Grimmke-Stiftung (to  
40 P.L.), from the Tschira-Foundation for InformaticsForLife to A.K.R. (research funding  
41 of C.M.), from the German Heart Foundation/German Foundation of Heart Research  
42 (Fellowship to A.K.R), from the German Internal Medicine Society (Clinician-Scientist-  
43 Program to A.K.R.), from the German Research Foundation (UL 466/2-1 to N.D.U.),  
44 and from the Joachim Siebeneicher Foundation (to D.T.).

45

46 **Disclosures:** C.M. acknowledges educational support from Biotronik and Johnson &  
47 Johnson, while A.K.R. acknowledges support from Boston Scientific, Johnson &  
48 Johnson, Abbott, and Medtronic. D.T. has received lecture fees/honoraria from various  
49 pharmaceutical and medical device companies, including Abbott, AstraZeneca, Bayer  
50 Vital, Boehringer Ingelheim Pharma, Bristol-Myers Squibb, Daiichi Sankyo, Johnson  
51 and Johnson Medical, Medtronic, Novartis, Pfizer Pharma, Sanofi-Aventis, and ZOLL  
52 CMS. P.L. has received lecture fees from Bayer Vital, Pfizer Pharma, and Bristol-  
53 Myers-Squibb, as well as educational support from Boston Scientific and  
54 fees/honoraria from Johnson & Johnson and Boston Scientific. The remaining authors  
55 have declared no relevant relationships.

**56 Abstract****57 Background**

58 Promising as a treatment option for life-threatening ventricular arrhythmias, cardiac  
59 stereotactic body radiotherapy (cSBRT) has demonstrated early antiarrhythmic effects  
60 within days of treatment. The mechanisms underlying the immediate and short-term  
61 antiarrhythmic effects are poorly understood.

**62 Objectives**

63 We hypothesize that cSBRT has a direct antiarrhythmic effect on cellular  
64 electrophysiology through reprogramming of ion channel and gap junction protein  
65 expression.

**66 Methods**

67 Following exposure to 20Gy of X-rays in a single fraction, neonatal rat ventricular  
68 cardiomyocytes (NRVCs) were analyzed 24 and 96h post-radiation to determine  
69 changes in conduction velocity, beating frequency, calcium transients, and action  
70 potential duration (APD) in both monolayers and single cells. Additionally, the  
71 expression of gap junction proteins, ion channels, and calcium handling proteins was  
72 evaluated at protein and mRNA levels.

**73 Results**

74 Following irradiation with 20Gy, NRVCs exhibited increased beat rate and conduction  
75 velocities 24 and 96h after treatment. mRNA and protein levels of ion channels were  
76 altered, with the most significant changes observed at the 96h-mark. Upregulation of  
77 *Cacna1c* (Ca<sub>v</sub>1.2), *Kcnd3* (K<sub>v</sub>4.3), *Kcnh2* (K<sub>v</sub>11.1), *Kcnq1* (K<sub>v</sub>7.1), *Kcnk2* (K<sub>2P</sub>2.1),  
78 *Kcnj2* (K<sub>ir</sub>2.1), and *Gja1* (Cx43) was noted, along with improved gap junctional  
79 coupling. Calcium handling was affected, with increased *Ryr2* (R<sub>YR</sub>2) and *Slc8a1*

80 (NCX) expression and altered properties 96h post-treatment. Fibroblast and  
81 myofibroblast levels remained unchanged.

## 82 **Conclusions**

83 cSBRT modulates expression of various ion channels, calcium handling proteins, and  
84 gap-junction proteins. The described alterations in cellular electrophysiology may be  
85 the underlying cause of the immediate antiarrhythmic effects observed following  
86 cSBRT.

Journal Pre-proof

87 **Keywords:** radiation; ion channel; remodeling; neonatal rat cardiomyocytes;  
88 ventricular arrhythmia, sudden cardiac death.

89

90 **Abbreviations list:**

91 APD=Action potential Duration

92 cSBRT=Cardiac stereotactic body radiation therapy

93 CV=Conduction velocity

94 Cx43=Connexin 43

95 FDHM=Full duration at half maximum

96 hiPSC-CMs=Human induced pluripotent stem cell-derived cardiomyocytes

97 ICD=Implantable cardioverter-defibrillator

98 NRVCs=Neonatal rat ventricular cardiomyocytes

99 Rx=Irradiation

100 TTP=Time-to-peak

101

102

103

104

105

106

## 107 **1. Introduction**

108 Scar-related ventricular arrhythmias are a significant cause of morbidity and mortality  
109 in patients with impaired cardiac function and structural heart disease, often leading  
110 to sudden cardiac death.<sup>1</sup> Cardiac stereotactic body radiotherapy (cSBRT) for the  
111 treatment of ventricular tachycardia (VT) and ventricular fibrillation in patients with  
112 arrhythmic events has been an emerging technology within the last years and has  
113 shown promising effects in terms of immediate reduction of ventricular arrhythmias  
114 and ICD-interventions.<sup>2</sup> The latency of expected reduction of VT burden after cSBRT  
115 is of utmost importance due to the life-threatening character of ventricular arrhythmias.  
116 The antiarrhythmic effects of cardiac irradiation are thought to include the induction of  
117 scar homogenization and fibrosis. However, clinical studies consistently show that  
118 irradiation has an early antiarrhythmic effect within days of treatment, i.e. before the  
119 onset of fibrosis.<sup>2-5</sup> The molecular processes responsible for this initial antiarrhythmic  
120 effect have not yet been fully resolved.

121 The effect of immediate reduction of VT-burden was observed after 25Gy single-  
122 fraction photon irradiation (Rx).<sup>2,4</sup> At present, there is a lack of information regarding  
123 the minimum radiation dosage required to achieve antiarrhythmic effects. Radiation  
124 dose is mainly derived from preclinical studies, proposing electrophysiologic effects at  
125 or above 24Gy due to the induction of fibrosis.<sup>4,6-8</sup> This collectively suggests the  
126 potential for electrical remodeling independent of the onset of fibrosis.<sup>2,4</sup>

127 VTs are typically a result of myocardial re-entry occurring in regions with  
128 inhomogeneous scarring or at the edges of scars.<sup>9</sup> This type of re-entry is made  
129 possible due to the local slowing of electrical conduction caused by fibrosis as well as  
130 a decrease in gap junction coupling.<sup>10</sup>



131 Little is known about the radiation-dependent effects at the molecular level of cardiac  
132 electrophysiology; repeatedly, alterations of the cardiac conduction protein connexin  
133 43 (Cx43) were described, but both up- and downregulation have been observed.<sup>11-15</sup>  
134 Recently an upregulation of Cx43 and the cardiac fast sodium channel Nav1.5 was  
135 found six weeks after 25Gy whole heart irradiation in a mouse model with and without  
136 myocardial infarction causing an increase in cardiac conduction velocity (CV)  
137 reprogramming that was also achieved at lower Rx doses of 15 and 20Gy.<sup>16</sup> After  
138 25Gy whole heart irradiation in rats, dynamic changes in the cardiac proteome,  
139 including proteins of the the cardiac conduction system were observed within one  
140 week.<sup>15</sup> Significant functional electrocardiographic changes were also observed in  
141 human induced pluripotent stem cell-derived cardiomyocytes (hiPSC-CMs) exposed  
142 to a single dose of X-rays of 20 to 50Gy.<sup>17,18</sup>

143 In the present study, we evaluated the mechanisms underlying the immediate  
144 antiarrhythmic effects of cSBRT. We hypothesized that radiation with less than 25Gy  
145 is sufficient to induce antiarrhythmic electrical remodeling.

146

147

148

149

150

151

152

153

## 154 **2. Methods**

155 Full experimental procedures and any associated references are available as  
156 Supplemental Material.

157

### 158 **2.1 Ethics statement**

159 Animal studies were conducted in accordance with the Guide for the Care and Use of  
160 Laboratory Animals as adopted and issued by the U.S. National Institutes of Health  
161 (NIH publication No. 85-23, revised 1985), and the current version of the German Law  
162 on the Protection of Animals was followed. This study conforms to Directive  
163 2010/63/EU of the European Parliament.

164

### 165 **2.2 Statistics**

166 Statistical analyses were conducted using GraphPad Prism 6.0 software and  
167 OriginPro 2022 software. Data are presented as box and whisker plots with confidence  
168 intervals (CI), and the number of experiments (n) is indicated in each section. We used  
169 the unpaired, two-tailed Student's t-test or Mann-Whitney U test for unequal variances  
170 and the paired Student's t-test for comparisons within experimental groups across  
171 different time points. Significance was denoted as \* $P < 0.05$ , \*\* $P < 0.01$ , \*\*\* $P < 0.001$ ,  
172 \*\*\*\* $P < 0.0001$ .

173

174

175

### 176 3. Results

#### 177 3.1 Irradiated NRVC monolayers showed higher conduction velocity, shortened 178 action potential duration, and increased beating frequency

179 We studied how Rx affects CV and action potential duration (APD) in NRVCs. At 24h  
180 after Rx, CV increased significantly (+30%,  $n=6$ ;  $P<0.0001$ ) (Fig. 1A). By 96h, CV was  
181 1.6-fold higher than in controls (+165%, Ctrl  $n=5$ , Rx  $n=6$ ,  $P=0.0014$ ) (Fig. 1D). APD  
182 did not differ significantly at 24h but shortened significantly by 96h (APD<sub>50</sub>: -52%, Ctrl  
183  $n=5$ , Rx  $n=6$ ;  $P<0.0001$ ; APD<sub>90</sub>: -50%, Ctrl  $n=5$ , Rx  $n=6$ ;  $P<0.001$ ) (Fig. 1E,F). Patch-  
184 clamp measurements at 24h showed APD<sub>90</sub> shortening (-11%,  $n=27$ ;  $P=0.026$ ). No  
185 significant apoptosis was observed at 24 or 96h after Rx (Fig. S1), and cardiac troponin  
186 T (cTnt) mRNA expression remained stable (Fig S2). At 24h, cultures were mainly  
187 cardiomyocytes with ~4% fibroblasts; fibroblast proliferation number increased by 96h  
188 with no significant differences between irradiated and non-irradiated cultures (+28%,  
189  $n=5$ ;  $P=0.469$ ) (Fig. S3). Irradiated cardiomyocytes showed an increase in beating  
190 frequency at 24h (+53%,  $n=6$ ;  $P=0.002$ ) and 96h (+59%, Ctrl  $n=8$ , Rx  $n=7$ ;  $P<0.001$ )  
191 post-Rx (Fig. 1G), with greater variability compared to controls.

#### 192 3.2 Ion channel remodeling after irradiation

193 We next examined radiation-induced electrophysiological remodeling at the molecular  
194 level and analysed differences in the expression of ion channel genes involved in the  
195 ventricular action potential by reverse transcription-quantitative polymerase chain  
196 reaction (RT-qPCR) analysis. At 24h after Rx, we found significant downregulation of  
197 the transcript levels of *Kcnq1/Kv7.1* ( $n=6$ ,  $P=0.036$ ) and *Kcnj8/Kir6.1* ( $n=6$ ,  $P=0.044$ )  
198 (Fig. 2A). Downregulation of *Kcnj8/Kir6.1* transcript persisted at 96h after Rx ( $n=6$ ,  
199  $P<0.0001$ ). In contrast, the transcript levels of *Cacna1c/Cav1.2* ( $n=6$ ,  $P=0.023$ ) and

200 the potassium channels *Kcnd3/K<sub>v</sub>4.3* ( $n=6$ ,  $P=0.0005$ ), *Kcnh2/K<sub>v</sub>11.1* ( $n=6$ ,  
201  $P<0.0001$ ), *Kcnq1/K<sub>v</sub>7.1* ( $n=6$ ,  $P<0.0001$ ), *Kcnk2/K<sub>2P</sub>2.1* ( $n=6$ ,  $P=0.032$ ), and  
202 *Kcnj2/K<sub>ir</sub>2.1* ( $n=6$ ,  $P=0.0001$ ) were significantly upregulated at 96h after Rx compared  
203 to those in control cultures. We found no differences in the expression of  
204 *Scn5a/Nav<sub>1.5</sub>*, *Kcne1/MinK*, and *Kcnk3/K<sub>2P</sub>3.1*. Western blotting of samples harvested  
205 at 96h after Rx confirmed the RT-qPCR results at the protein level (Fig. 2B, C).

### 206 **3.3 Irradiation improves intercellular coupling by upregulation of Cx43 and** 207 **increased gap junction formation**

208 To assess study effects of Rx on gap junctional coupling we assessed Cx43  
209 expression (Fig. 3). At 24h after Rx, there were no significant changes in Cx43 mRNA  
210 ( $P=0.316$ ) (Fig. 3A) or protein levels ( $P=0.890$ ) (Fig. 3B, C). However, by 96h, both  
211 Cx43 mRNA ( $P<0.0001$ ) and protein levels were upregulated ( $P<0.0001$ ) (Fig. 3A, C).  
212 Immunostaining revealed a 45% increase in Cx43 expression at cell-to-cell contact  
213 zones in irradiated cardiomyocytes ( $P<0.0001$ ) (Fig. 3D), indicating increased gap  
214 junction formation. Functional evaluation using fluorescence recovery after  
215 photobleaching showed significantly faster fluorescence recovery in irradiated  
216 cardiomyocytes (+24%,  $P=0.041$ ), indicating enhanced functional gap junctions (Fig.  
217 3E-G).

### 218 **3.4 Irradiated neonatal rat ventricular cardiomyocytes showed altered calcium** 219 **handling.**

220 Calcium handling changes may affect CV and APD. Using IonOptix, we measured  
221 calcium transients (Fig. 4). At 24h, diastolic calcium increased in irradiated monolayers  
222 (+7%,  $P=0.0003$ ) (Fig. 4B), together with a reduced time-to peak (TTP) and full  
223 duration at half maximum (FDHM) and time to peak (TTP; -26% and -23%,

224 respectively;  $P < 0.0001$ ) (Fig. 4B). At 96h, diastolic calcium remained elevated (+11%,  
225  $P = 0.0004$ ), with further reductions in FDHM and TTP (-30% and -23%, respectively;  
226  $P < 0.0001$ ) (Fig. 4D). Additionally, irradiated cardiomyocytes displayed increased  
227 calcium transient amplitudes and faster decay rates after 96h.

228 RT-qPCR and western blot analysis of genes involved in cardiac calcium handling  
229 (Fig. 5) showed an increase in PLN mRNA at 24h after Rx ( $P = 0.012$ ), which further  
230 increased by 96h ( $P < 0.001$ ), along with an increase in PLN protein ( $P = 0.008$ ). NCX  
231 mRNA and protein levels rose at 96h post-Rx as well as RyR2 mRNA ( $P = 0.005$ ). No  
232 significant changes were observed in CaMKII $\delta$  and CaMKII $\gamma$  mRNA and protein levels  
233 at 24 or 96h after Rx.

### 234 **3.5 Effects of irradiation on extracellular matrix**

235 Next, we investigated the effect of irradiation on extracellular matrix formation and  
236 conversion of fibroblasts to paracrine active myofibroblasts in mixed cultures of  
237 cardiomyocytes and fibroblasts. The fibroblast-to-myofibroblast switch is accompanied  
238 by increases in the expression of  $\alpha$ -smooth muscle actin ( $\alpha$ -SMA) and the production  
239 of extracellular matrix components, a key event in connective tissue remodeling. As  
240 shown by western blotting, Rx did not significantly increase  $\alpha$ -SMA or vimentin protein  
241 levels (Fig. 6).

242

243

244

245

246

247

#### 248 4. Discussion

249 We investigated cSBRT's antiarrhythmic effects in NRVC cultures. A single Rx-dose  
250 of 20Gy led to an immediate rise in beat rate and CV, alongside significant APD  
251 shortening. We also observed changes in the expression of genes encoding ion  
252 channel and calcium handling proteins, notably at 96h post-Rx. These findings support  
253 the notion of an early antiarrhythmic impact preceding tissue damage. This study  
254 represents the first systematic exploration of cSBRT's immediate antiarrhythmic  
255 effects, highlighting the role of ion channels, gap junctional coupling, and calcium  
256 homeostasis in modifying cellular electrophysiology.

#### 257 Irradiation affects electrophysiology in cardiomyocytes

258 In irradiated cardiomyocytes, there was a significant increase in beating frequency  
259 compared to the unirradiated group, possibly due to increased diastolic calcium levels.  
260 Mouse embryonic stem cells irradiated with 5Gy of  $\gamma$ -rays exhibited altered contractile  
261 properties and reduced beating frequency after differentiation into cardiomyocytes.<sup>20</sup>  
262 This discrepancy may be explained by the use of different experimental models, but  
263 could also suggest a dose-dependent effect.

264 Rx caused changes in the expression of cardiac ion channels directly affecting  
265 membrane excitability. Rx induced downregulation of *Kcnj8/K<sub>ir</sub>6.1* that persisted for  
266 96h. *Cacna1c/Ca<sub>v</sub>1.2* and the potassium channels *Kcnd3/K<sub>v</sub>4.3*, *Kcnh2/K<sub>v</sub>11.1*,  
267 *Kcnk2/K<sub>2P</sub>2.1*, and *Kcnj2/K<sub>ir</sub>2.1* showed significant upregulation at 96h after Rx.  
268 *Kcnq1/K<sub>v</sub>7.1* exhibited biphasic regulation with reduced expression at 24h and  
269 increased expression after 96h. Collectively, the changes in repolarizing potassium  
270 channel expression are suspected to shorten APD and to contribute to an increased  
271 CV. Exposure of iPSC-CMs to 20Gy did not lead to significant upregulation of *KCND3*,

272 *KCNH2*, *SCN5A*, *CACNA1C* or *GJA1* after 7 days in contrast to Rx doses of 25 or  
273 30Gy.<sup>18</sup> Interestingly, another research group reported a significant increase in Nav1.5  
274 density six weeks after whole heart irradiation of mice with 20Gy.<sup>16</sup> This disparity may  
275 be explained by compensatory mechanisms or dynamic changes that occur following  
276 irradiation, as indicated by large-scale proteomic analysis three and seven days after  
277 2- and 25-Gy Rx.<sup>15</sup> These alterations resulted in APD shortening at 24h after Rx. This  
278 observation is consistent with our optical voltage mapping results, demonstrating  
279 increased CV and consistent APD shortening in irradiated NRVC monolayers.

### 280 **Irradiation improves impulse propagation and conduction velocity**

281 Our data showed upregulation of Cx43 and improved gap junction coupling in NRVCs  
282 at 96h after Rx, which can also in part explain the increased CV. Previous studies  
283 have reported that Cx43 expression is very sensitive to ionizing radiation in various  
284 cell lines.<sup>21-24</sup> Our study adds to this observation and confirms the hypothesis that the  
285 induced Cx43 proteins form functional channels. There are also contrary observations  
286 in the field, whose cause has not been clarified. Kim et al. showed a non-significant  
287 trend towards an increase in Cx43 mRNA following 20-Gy Rx of hiPSC-CMs.<sup>18</sup> Cha et  
288 al. even reported a reduction in Cx43 expression two and three weeks after irradiation  
289 with 20 to 50Gy by immunostaining of adult rat hearts.<sup>17</sup> The latter result is at odds  
290 with the observation that cardiac-specific postnatal loss of Cx43 slowed ventricular CV  
291 and increased the susceptibility to spontaneous ventricular arrhythmias and sudden  
292 cardiac death.<sup>25</sup> Moreover, other preclinical studies also found increased cell-to-cell  
293 conduction via Cx43 upregulation upon 25Gy irradiation.<sup>11-14</sup> To our understanding,  
294 the inconsistencies in the field may arise from differences between animal models,  
295 type of radiation, and dose or timepoint of evaluation. Further studies are needed to  
296 address these different observations.

297 **Calcium homeostasis and calcium handling proteins are affected by single dose**  
298 **irradiation**

299 Regarding calcium handling proteins, significant upregulation of PLN,  
300 *Cacna1c*/ $Ca_v1.2$ , RYR2, and NCX mRNA and protein levels was detected after  
301 exposure of NRVCs to 20Gy. Kim et al.<sup>15</sup> reported an increase in RYR2 protein three  
302 days after exposure of adult rats to 25Gy, which is consistent with our findings. As  
303 mentioned previously, there are also reports indicating no significant changes in  
304 CACNA1C expression following 20-Gy irradiation,<sup>18</sup> a phenomenon that remains  
305 unexplained.

306 At the functional level, a variety of changes in the calcium transient properties were  
307 observed. We found persistently elevated radiation-dependent diastolic calcium  
308 levels. To our understanding this increase might arise from radiation-induced oxidative  
309 stress and reactive oxygen species (ROS) formation<sup>26</sup> leading to calcium leakage from  
310 the sarcoplasmic reticulum, as proposed previously.<sup>27</sup> However, we did not measure  
311 ROS formation in our model as this was not the scope of the present study. At 24 and  
312 96h after Rx, we found faster kinetics of calcium transients as evidence by a reduction  
313 of TTP and FDHM. At 96h after Rx, calcium transients also showed increased  
314 amplitudes and faster decay rates. The increased amplitude may be associated with  
315 the observed upregulation of *Cacna1c*/ $Ca_v1.2$  and RyR2. The faster decay rate might  
316 be related to the increased abundance of NCX. In a comprehensive study<sup>27</sup>, Sag et al.  
317 assessed the acute (1h after irradiation) and chronic (one week after irradiation)  
318 effects of 20-Gy mediastinal photon radiation on calcium handling in murine  
319 cardiomyocytes. The investigation demonstrated an immediate elevation in calcium  
320 transient amplitudes post-irradiation, as opposed to a sustained reduction in the  
321 chronic phase. In contrast to our findings, the authors described an acute and chronic



322 irradiation-dependent activation of CaMKII due to increased oxidative stress.<sup>27</sup> In our  
323 study, CaMKII $\delta$  and CaMKII $\gamma$  levels were not affected by Rx. Also, while we found an  
324 increase in Slc8a1 (NCX) expression and no change in Atp2a1 (SERCA) mRNA (Fig.  
325 5) after Rx, in the study by Sag et al. NCX remained unchanged and SERCA2a  
326 expression was decreased on week after Rx. We focused on the short-term effects up  
327 to 96h post-Rx, leaving uncertainty regarding the normalization or exacerbation of  
328 expression differences over time. However, both studies highlight the influence of  
329 ionizing radiation on cardiac calcium handling, urging further research to grasp its  
330 implications for antiarrhythmic effects.

### 331 **Significance for antiarrhythmic therapy**

332 In most heart diseases, re-entry mechanisms are based on remodeling processes  
333 causing (local) conduction slowing.<sup>28</sup> Our data support early antiarrhythmic effects  
334 through reprogramming of ion channels causing an increase in CV and APD  
335 shortening in irradiated cardiomyocytes. These results are consistent with a study of  
336 Anyukhovskiy et al., which showed antiarrhythmic effects of improving the conduction  
337 in slow conducting arrhythmogenic mouse tissue by Scn4a (Nav1.4) or Gjb1 (connexin  
338 32) gene transfer.<sup>29</sup> Shortening of the effective refractory period of the targeted  
339 myocardium could lead to enhanced local conduction<sup>30</sup> and consequently, the re-entry  
340 phenomenon would decrease through an electrical homogenization. As a therapeutic  
341 approach, this could already demonstrate strong antiarrhythmic effects.<sup>31,32</sup> The  
342 described effects of abolishing inhomogeneities and delayed conduction properties  
343 within the scar, partially achieved through altered ion channel expressions and  
344 improved gap junctional coupling, may represent a potentially effective antiarrhythmic  
345 concept in the treatment of ventricular tachycardias in patients with scar-related  
346 mechanisms. These effects occur independently of the formation of fibrous scars,

347 suggesting that these electrical changes can already be effectively observed at lower  
348 radiation doses. Further work in disease models will be essential to understand  
349 whether the response of the diseased myocardium is similar to that of healthy tissue.

350 Although the antiarrhythmic mechanisms of Rx remain to be determined, several  
351 studies showed early myocardial effects in a dose-dependent manner.<sup>15-18</sup> A  
352 persistent observation is that 20Gy is sufficient to achieve electrophysiological  
353 remodeling, although it remains unclear if those effects are long-lasting as suggested  
354 by our data. The currently used dose of 25Gy in patients was initially chosen to imitate  
355 the effects seen after radiofrequency ablation. Currently, ~81% of the patients  
356 receiving SBRT suffer from mild adverse effects<sup>2,4</sup>, which highlights the importance of  
357 improving its safety through dose reduction. The reported data give a mechanistic  
358 insight into fast antiarrhythmic changes and underline the option for dose reduction  
359 without loss of efficacy. Initial clinical reports support effective antiarrhythmic treatment  
360 with a radiation dose even below 20Gy.<sup>33</sup>

### 361 **Potential limitations and future directions**

362 This study has several noteworthy limitations. We chose not to inhibit fibroblasts to  
363 better mimic the extracellular environment, which could impact the results as  
364 fibroblasts influence cardiomyocyte electrophysiology through heterocellular coupling.  
365 Neonatal cardiomyocytes were selected for patch-clamp investigations, with the  
366 present work focusing on a descriptive analysis of electrophysiological properties  
367 within a maximum of 96h post-irradiation. Further studies in a disease model are  
368 needed to enable the examination of adult cells over a longer observation period. Our  
369 model does not replicate diseased hearts, which significantly affects the causal  
370 interpretation of the results. Additionally, we used photon irradiation, but other

371 energies like protons or heavy ions may yield different effects and warrant  
372 investigation.<sup>34,35</sup>

373

## 374 **5. Conclusion**

375 Our results indicate an association of acute irradiation effects and electrophysiological  
376 remodeling in cardiomyocytes. Changes of cellular ion channel expression, calcium  
377 homeostasis and cell-cell-propagation lead to electrophysiological changes. Although  
378 the final mechanism causing antiarrhythmic changes remains to be discovered, these  
379 results reveal new insight into acute antiarrhythmic effects of cSBRT therapy on  
380 cardiomyocytes .

381

## 382 **6. Acknowledgement**

383 We declare that no artificial intelligence (AI) was used in preparation of the present  
384 manuscript.

385 We gratefully acknowledge the excellent technical assistance of Axel Schöffel, Teresa  
386 Caspari, Patrizia Lo Vetere, Nicole Westerhorstmann and Miriam Baier.

387

388 **7. References**

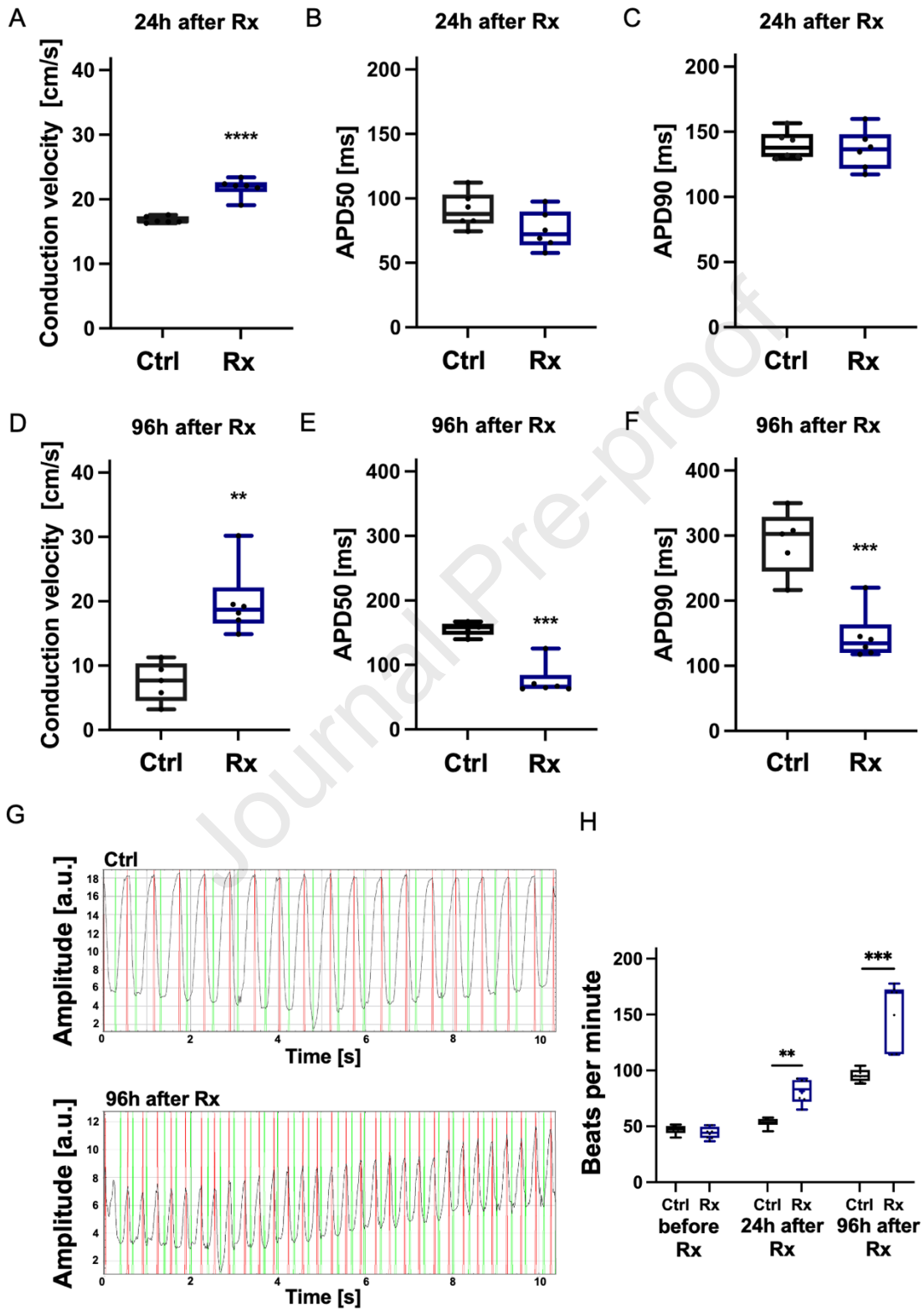
- 389 1. Zeppenfeld K, Tfelt-Hansen J, de Riva M, et al.: 2022 ESC Guidelines for the  
390 management of patients with ventricular arrhythmias and the prevention of  
391 sudden cardiac death: Developed by the task force for the management of  
392 patients with ventricular arrhythmias and the prevention of sudden cardiac death  
393 of the European Society of Cardiology (ESC) Endorsed by the Association for  
394 European Paediatric and Congenital Cardiology (AEPC). *European Heart Journal*  
395 2022; 43:3997–4126.
- 396 2. Kovacs B, Mayinger M, Schindler M, Steffel J, Andratschke N, Saguner AM:  
397 Stereotactic radioablation of ventricular arrhythmias in patients with structural  
398 heart disease - A systematic review. *Radiother Oncol* 2021; 162:132–139.
- 399 3. Ninni S, Gallot-Lavallée T, Klein C, et al.: Stereotactic Radioablation for  
400 Ventricular Tachycardia in the Setting of Electrical Storm. *Circ Arrhythm*  
401 *Electrophysiol* 2022; 15:e010955.
- 402 4. van der Ree MH, Blanck O, Limpens J, et al.: Cardiac radioablation—A  
403 systematic review. *Heart Rhythm Elsevier*, 2020; 17:1381–1392.
- 404 5. Robinson CG, Samson, Moore, et al.: Phase I/II Trial of Electrophysiology-Guided  
405 Noninvasive Cardiac Radioablation for Ventricular Tachycardia. *Circulation*  
406 American Heart Association, 2018; 139:313–321.
- 407 6. Blanck O, Bode F, Gebhard M, et al.: Dose-escalation study for cardiac  
408 radiosurgery in a porcine model. *Int J Radiat Oncol Biol Phys* 2014; 89:590–598.
- 409 7. Chang JH, Cha M-J, Seo J-W, et al.: Feasibility study on stereotactic radiotherapy  
410 for total pulmonary vein isolation in a canine model. *Sci Rep* 2021; 11:12369.
- 411 8. Lehmann HI, Richter D, Prokesch H, et al.: Atrioventricular node ablation in  
412 Langendorff-perfused porcine hearts using carbon ion particle therapy: methods  
413 and an in vivo feasibility investigation for catheter-free ablation of cardiac  
414 arrhythmias. *Circ Arrhythm Electrophysiol* 2015; 8:429–438.
- 415 9. de Chillou C, Lacroix D, Klug D, et al.: Isthmus characteristics of reentrant  
416 ventricular tachycardia after myocardial infarction. *Circulation* 2002; 105:726–  
417 731.
- 418 10. de Bakker JM, van Capelle FJ, Janse MJ, et al.: Slow conduction in the infarcted  
419 human heart. “Zigzag” course of activation. *Circulation* 1993; 88:915–926.
- 420 11. Amino M, Yoshioka K, Tanabe T, et al.: Heavy ion radiation up-regulates Cx43  
421 and ameliorates arrhythmogenic substrates in hearts after myocardial infarction.  
422 *Cardiovasc Res Oxford Academic*, 2006; 72:412–421.
- 423 12. Amino M, Yoshioka K, Fujibayashi D, et al.: Year-long upregulation of connexin43  
424 in rabbit hearts by heavy ion irradiation. *Am J Physiol Heart Circ Physiol* 2010;  
425 298:H1014-1021.

- 426 13. Viczenczova C, Szeiffova Bacova B, Egan Benova T, et al.: Myocardial connexin-  
427 43 and PKC signalling are involved in adaptation of the heart to irradiation-  
428 induced injury: Implication of miR-1 and miR-21. *Gen Physiol Biophys* 2016;  
429 35:215–222.
- 430 14. Viczenczova C, Kura B, Egan Benova T, et al.: Irradiation-Induced Cardiac  
431 Connexin-43 and miR-21 Responses Are Hampered by Treatment with  
432 Atorvastatin and Aspirin. *International Journal of Molecular Sciences*  
433 Multidisciplinary Digital Publishing Institute, 2018; 19:1128.
- 434 15. Kim BH, Jung JW, Han D, Cha M-J, Chang JH: One-Week Dynamic Changes in  
435 Cardiac Proteomes After Cardiac Radioablation in Experimental Rat Model. *Front*  
436 *Cardiovasc Med* 2022; 9:898222.
- 437 16. Zhang DM, Navara R, Yin T, et al.: Cardiac radiotherapy induces electrical  
438 conduction reprogramming in the absence of transmural fibrosis. *Nat Commun*  
439 2021; 12:5558.
- 440 17. Cha M-J, Seo J-W, Kim HJ, et al.: Early Changes in Rat Heart After High-Dose  
441 Irradiation: Implications for Antiarrhythmic Effects of Cardiac Radioablation. *J Am*  
442 *Heart Assoc* 2021; 10:e019072.
- 443 18. Kim JS, Choi SW, Park Y-G, et al.: Impact of High-Dose Irradiation on Human  
444 iPSC-Derived Cardiomyocytes Using Multi-Electrode Arrays: Implications for the  
445 Antiarrhythmic Effects of Cardiac Radioablation. *Int J Mol Sci* 2021; 23:351.
- 446 19. Grune T, Ott C, Häseli S, Höhn A, Jung T: The “MYOCYTER” – Convert cellular  
447 and cardiac contractions into numbers with ImageJ. *Sci Rep Nature Publishing*  
448 *Group*, 2019; 9:15112.
- 449 20. Rebuzzini P, Fassina L, Mulas F, et al.: Mouse embryonic stem cells irradiated  
450 with  $\gamma$ -rays differentiate into cardiomyocytes but with altered contractile  
451 properties. *Mutat Res* 2013; 756:37–45.
- 452 21. Sottas V, Wahl C-M, Trache MC, et al.: Improving electrical properties of iPSC-  
453 cardiomyocytes by enhancing Cx43 expression. *Journal of Molecular and Cellular*  
454 *Cardiology* 2018; 120:31–41.
- 455 22. Glover D, Little JB, Lavin MF, Gueven N: Low dose ionizing radiation-induced  
456 activation of connexin 43 expression. *International Journal of Radiation Biology*  
457 *Taylor & Francis*, 2003; 79:955–964.
- 458 23. Banaz-Yaşar F, Tischka R, Iliakis G, Winterhager E, Gellhaus A: Cell Line  
459 Specific Modulation of Connexin43 Expression after Exposure to Ionizing  
460 Radiation. *Cell Communication & Adhesion Taylor & Francis*, 2005; 12:249–259.
- 461 24. Azzam EI, de Toledo SM, Little JB: Expression of CONNEXIN43 is highly  
462 sensitive to ionizing radiation and other environmental stresses. *Cancer Res*  
463 2003; 63:7128–7135.

- 464 25. Gutstein DE, Morley GE, Tamaddon H, et al.: Conduction slowing and sudden  
465 arrhythmic death in mice with cardiac-restricted inactivation of connexin43. *Circ*  
466 *Res* 2001; 88:333–339.
- 467 26. Kim W, Lee S, Seo D, et al.: Cellular Stress Responses in Radiotherapy. *Cells*  
468 Multidisciplinary Digital Publishing Institute, 2019; 8:1105.
- 469 27. Sag CM, Wolff HA, Neumann K, et al.: Ionizing radiation regulates cardiac Ca  
470 handling via increased ROS and activated CaMKII. *Basic Res Cardiol* 2013;  
471 108:385.
- 472 28. Holmes JW, Laksman Z, Gepstein L: Making better scar: Emerging approaches  
473 for modifying mechanical and electrical properties following infarction and  
474 ablation. *Progress in Biophysics and Molecular Biology* 2016; 120:134–148.
- 475 29. Anyukhovskiy EP, Sosunov EA, Kryukova YN, et al.: Expression of skeletal  
476 muscle sodium channel (Nav1.4) or connexin32 prevents reperfusion arrhythmias  
477 in murine heart. *Cardiovasc Res* 2011; 89:41–50.
- 478 30. Roell W, Lewalter T, Sasse P, et al.: Engraftment of connexin 43-expressing cells  
479 prevents post-infarct arrhythmia. *Nature* 2007; 450:819–824.
- 480 31. Greener ID, Sasano T, Wan X, et al.: Connexin43 gene transfer reduces  
481 ventricular tachycardia susceptibility after myocardial infarction. *J Am Coll Cardiol*  
482 2012; 60:1103–1110.
- 483 32. Lau DH, Clausen C, Sosunov EA, et al.: Epicardial border zone overexpression  
484 of skeletal muscle sodium channel SkM1 normalizes activation, preserves  
485 conduction, and suppresses ventricular arrhythmia: an in silico, in vivo, in vitro  
486 study. *Circulation* 2009; 119:19–27.
- 487 33. Huang S-H, Wu Y-W, Shueng P-W, et al.: Case report: Stereotactic body radiation  
488 therapy with 12 Gy for silencing refractory ventricular tachycardia. *Front*  
489 *Cardiovasc Med* 2022; 9:973105.
- 490 34. Takami M, Hara T, Okimoto T, et al.: Electrophysiological and Pathological Impact  
491 of Medium-Dose External Carbon Ion and Proton Beam Radiation on the Left  
492 Ventricle in an Animal Model. *J Am Heart Assoc* 2021; 10:e019687.
- 493 35. Rapp F, Simoniello P, Wiedemann J, et al.: Biological Cardiac Tissue Effects of  
494 High-Energy Heavy Ions – Investigation for Myocardial Ablation. *Scientific*  
495 *Reports Nature Publishing Group*, 2019; 9:5000.

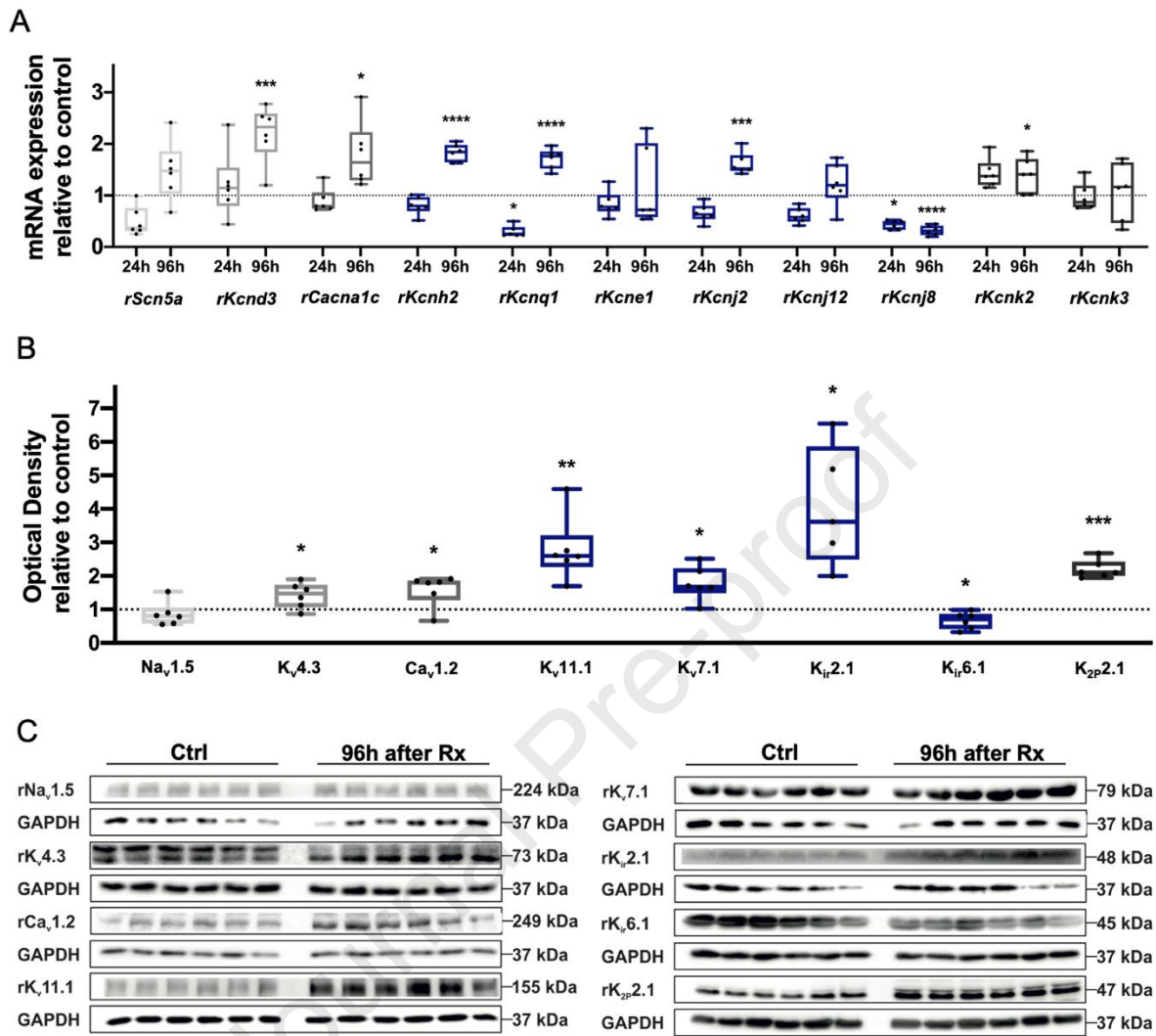
496

497

498 **8. Figures**499 **Figure 1**

500



501 **Figure 2**

502

503

504

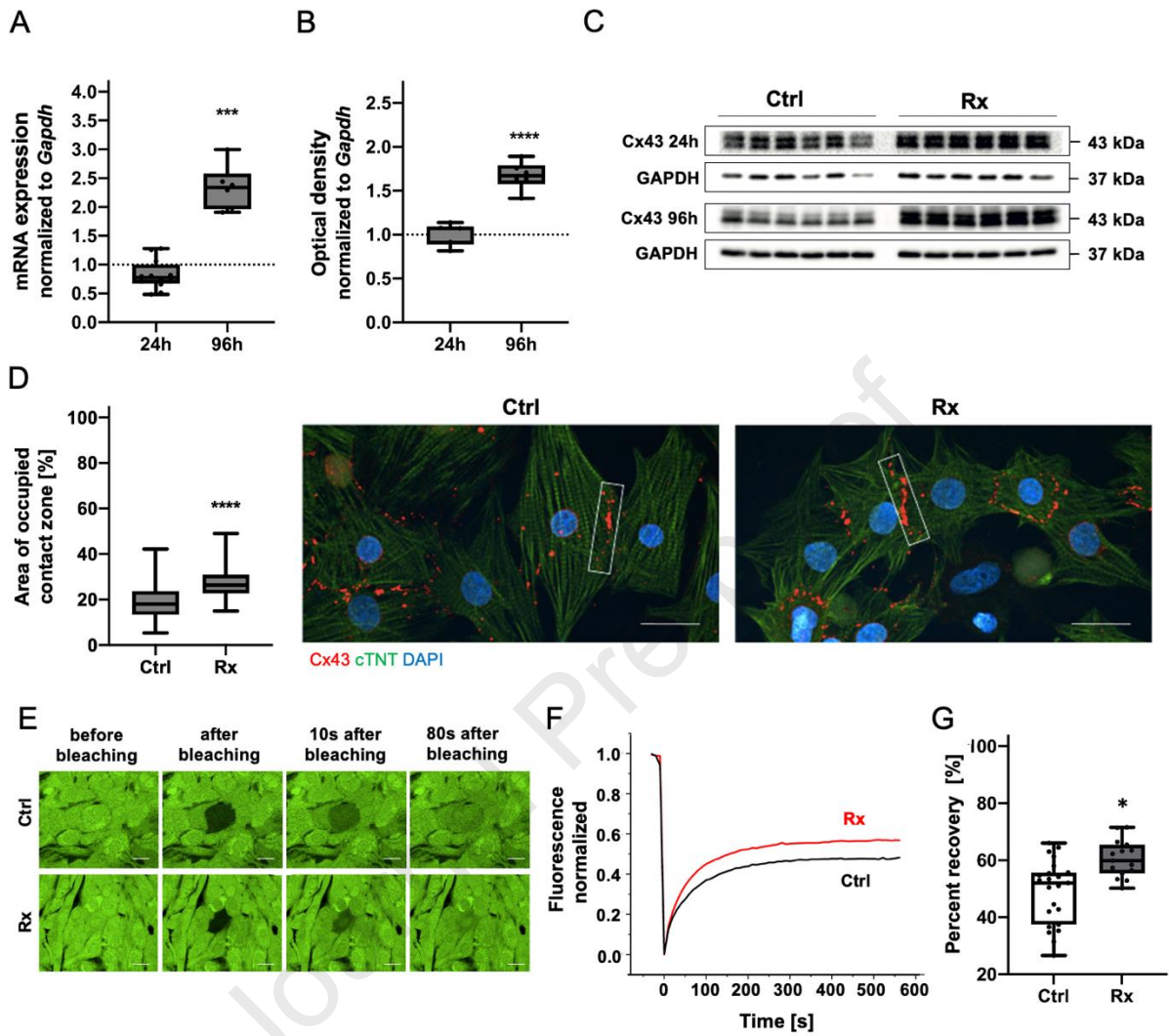
505

506

507

508



509 **Figure 3**

510

511

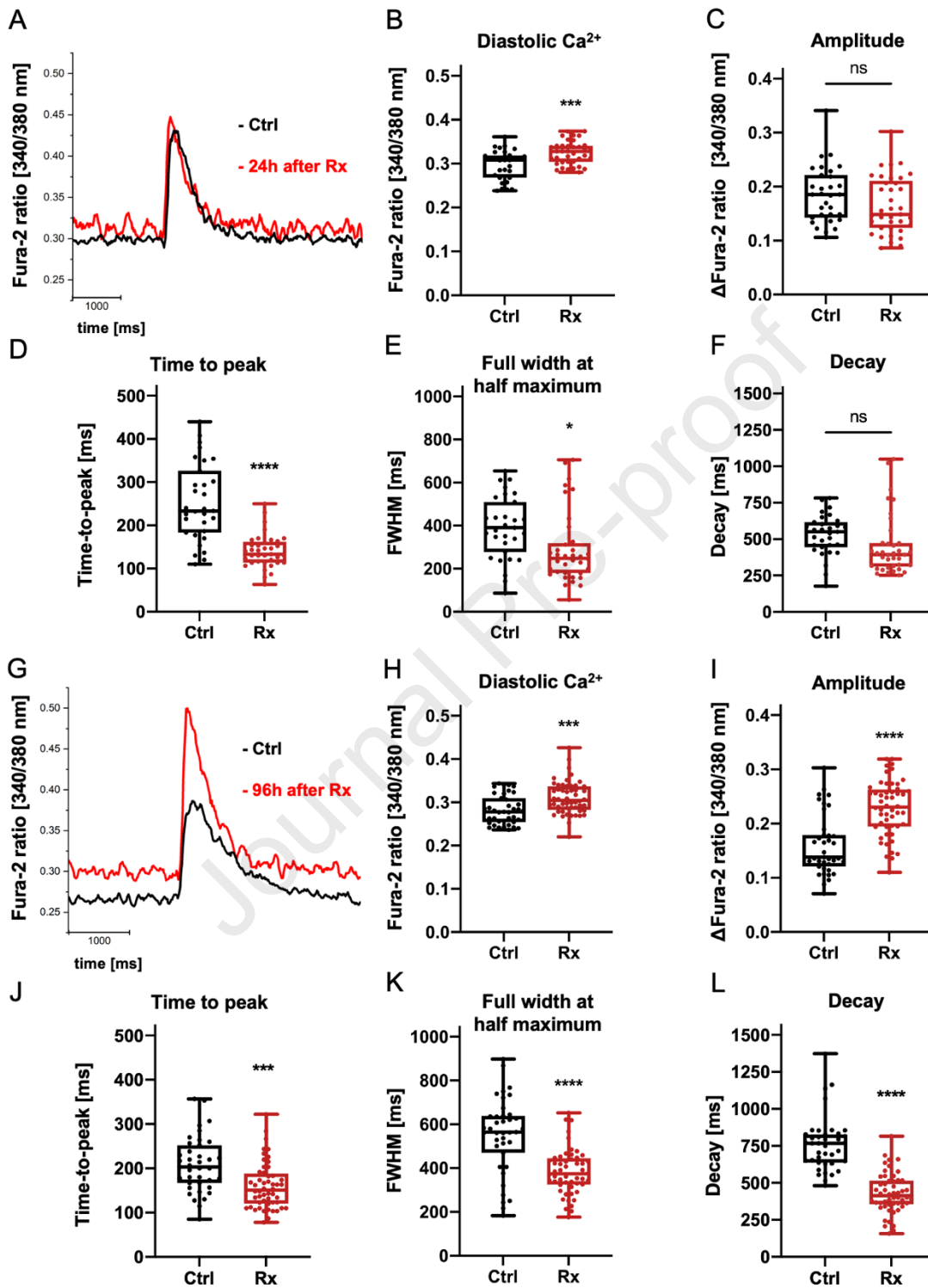
512

513

514

515

516

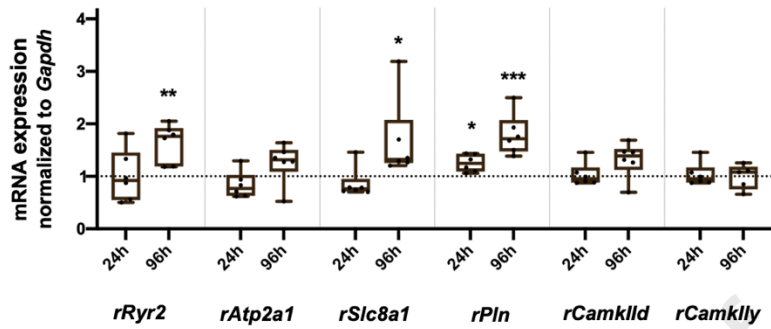
517 **Figure 4**

518

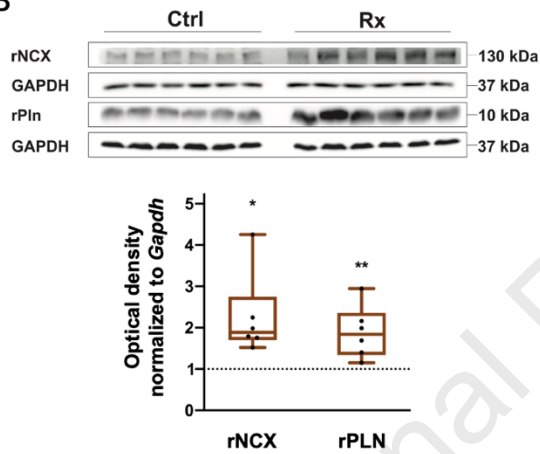
519

520 **Figure 5**

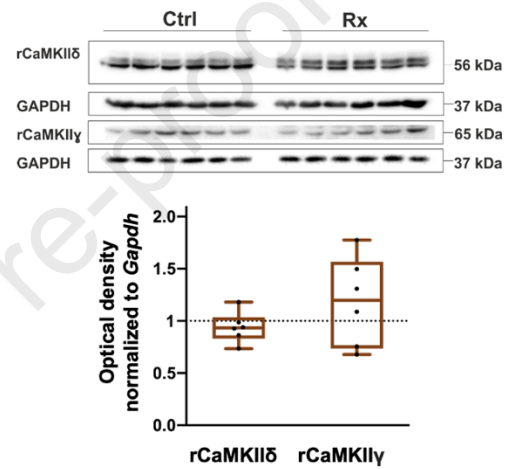
A



B



C



521

522

523

524

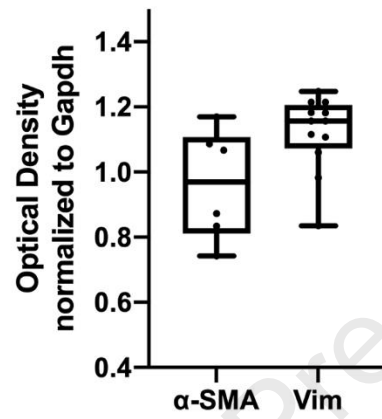
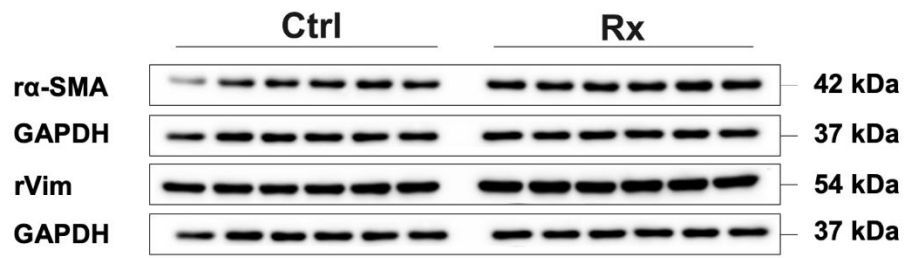
525

526

527

528

529

530 **Figure 6**

531

532

## 533 9. Figure legends

534 **Graphical abstract:** Overview of methods and major findings affecting the cellular  
535 electrophysiology 96h after 20Gy photon irradiation.

536 **Fig.1: Irradiated NRVC monolayers showed significantly increased conduction**  
537 **velocity and increased beating frequency.** A-F: Optical voltage mapping  
538 experiments of control and irradiated monolayers. (A, D) Conduction velocity (CV), (B,  
539 E) action potential duration at 50% repolarisation (APD<sub>50</sub>), and (C, F) action potential  
540 duration at 90% repolarization (APD<sub>90</sub>) of control (Ctrl) and irradiated monolayers 24h  
541 (A-C) or 96h (D-F) after irradiation (Rx) (Ctrl,  $n=5$  and  $6$ , respectively; Rx,  $n=6$ ) (G- H:  
542 Video Analysis of beating frequency using the Macro Myocyte for ImageJ with (G)  
543 representative contraction curves of a control and an irradiated cardiomyocyte 96h  
544 after Rx and (H) analysis of beating frequency before Rx (Ctrl  $n=6$ ; Rx,  $n=8$ ), 24h after  
545 Rx ( $n=6$ , each) and 96h after Rx (Ctrl  $n=8$ ; Rx,  $n=7$ ). Data are shown as box and  
546 whisker plots. (\* $p<0.05$ , \*\* $p<0.01$ , \*\*\* $p<0.001$ , \*\*\*\* $p<0.0001$ ).

547 **Fig.2: Radiation-induced ion channel remodeling 24 and 96h after Rx.** (A) mRNA  
548 transcripts of ion channels of the ventricular action potential 24 and 96h after Rx ( $n=6$ ,  
549 each). Representative western blots of ion channels 96 h after Rx compared to Ctrl  
550 and corresponding analysis of optical density are shown ( $n=6$ , each; B and C). Data  
551 are represented as box and whisker plots. (\* $p<0.05$ , \*\* $p<0.01$ , \*\*\* $p<0.001$ ).

552 **Fig.3: Irradiation increased cardiac cell-to-cell coupling.** (A) RT-qPCRs 24 and  
553 96h after Rx ( $n=12$ , each). Western blot results 24 (B) and 96h after Rx (C) ( $n=6$ ,  
554 each). (D) Quantification of the Cx43-area occupied relative to the membrane contact  
555 area 96h after Rx (Ctrl,  $n=113$ ; Rx  $n=115$ ). (E) Representative immunofluorescent  
556 stainings of Cx43 (red), cTnT (green) and DAPI (blue). A white box indicates the

557 location of Cx43 at the membrane contact area between neighbouring cells (scale  
558 bar=25 $\mu$ m). (E) Representative FRAP experiments with control and irradiated  
559 monolayers 96h after Rx (SB=25 $\mu$ m). (F) Average time courses of FRAP and (G)  
560 analysis of percent recovery 96h after Rx (Ctrl,  $n=23$ ; Rx,  $n=15$ ). Data are shown as  
561 box and whisker plots. (\* $p<0.05$ , \*\*\* $p<0.001$ , \*\*\*\* $p<0.0001$ ).

562 **Fig.4: Calcium transient analysis 24 and 96h after Rx.** (A) and (G): Representative  
563 traces of control (black) and irradiated monolayers (red) 24 (A) and 96h after Rx (G).  
564 Analysis of diastolic calcium, peak amplitude, time-to-peak (TTP), full duration at half  
565 maximum (FDHM) and decay 24h after Rx (Ctrl,  $n=31$ ; Rx,  $n=37$ ). Analysis of diastolic  
566 calcium, peak amplitude, TTP, FDHM and decay 96h after Rx (Ctrl,  $n=39$ ; Rx,  $n=52$ ).  
567 Data are shown as box and whisker plots. (\* $p<0.05$ , \*\* $p<0.01$ , \*\*\* $p<0.001$ ,  
568 \*\*\*\* $p<0.0001$ ).

569 **Fig.5: RT-qPCR and western blotting results of calcium handling proteins.** (A)  
570 Changes in the mRNA transcripts of RYR2, SERCA (Atp2a1), NCX (Slc8a1), PLN and  
571 CaMKIId and CaMKIIy at 24 and at 96h after Rx ( $n=6$ , each). (B) Western blotting of  
572 NCX and PLN 96h after Rx ( $n=6$ , each). (C) Western blotting of CaMKII $\delta$  and CaMKIIy  
573 96 h after Rx ( $n=6$ , each). Data are shown as box and whisker plots. (\* $p<0.05$ ,  
574 \*\* $p<0.01$ , \*\*\* $p<0.001$ ).

575 **Fig.6: Irradiation did not affect structural features of cardiac fibroblasts in mixed**  
576 **cardiomyocyte and fibroblast cultures.** Western blotting of  $\alpha$ -SMA and vimentin  
577 (Vim) 96h after Rx with respective blots shown and analysis of optical density ( $n=6$ ,  
578 each). Data are shown as box and whisker plots relative to Ctrl.

579

## **Supplemental Material**

### **Cardiac stereotactic body radiotherapy to treat malignant ventricular arrhythmias directly affects the cardiomyocyte electrophysiology**

**Authors:** Christine Mages, MD <sup>a,b,c,d#</sup>, Heike Gampp <sup>a,b#</sup>, Ann-Kathrin Rahm, MD <sup>a,b,c,d</sup>, Juline Hackbarth <sup>a,b</sup>, Julia Pfeiffer <sup>a,b</sup>, Finn Petersenn <sup>a,b</sup>, Xenia Kramp <sup>a,b</sup>, Fatemeh Kermani <sup>e</sup>, Juan Zhang, PhD <sup>f</sup>, Daniel Pijnappels, PhD <sup>f</sup>, Antoine A. F de Vries, PhD <sup>f</sup>, Katharina Seidensaal, MD <sup>g,h</sup>, Bernhard Rhein, PhD <sup>g,h</sup>, Jürgen Debus, MD <sup>g,h</sup>, Nina D. Ullrich, PhD <sup>c,e,i</sup>, Norbert Frey, MD <sup>a,b,c,d</sup>, Dierk Thomas, MD <sup>a,b,c</sup>, Patrick Lugenbiel, MD <sup>a,b,c\*</sup>

<sup>a</sup>Department of Cardiology, University Hospital Heidelberg, Heidelberg, Germany;

<sup>b</sup>Heidelberg Center for Heart Rhythm Disorders (HCR), University Hospital Heidelberg, Heidelberg, Germany;

<sup>c</sup>German Centre for Cardiovascular Research (DZHK), Partner site Heidelberg/Mannheim, University of Heidelberg, Heidelberg, Germany;

<sup>d</sup>Informatics4Life Consortium (Institute for Informatics Heidelberg), Heidelberg, Germany;

<sup>e</sup>Division of Cardiovascular Physiology, Institute of Physiology and Pathophysiology, Heidelberg, Germany;

<sup>f</sup>Department of Cardiology, Leiden University Medical Center, Leiden, the Netherlands

<sup>g</sup>Department of Radiation Oncology, Heidelberg University Hospital, Heidelberg, Germany;

<sup>h</sup>Heidelberg Institute of Radiation Oncology (HIRO), Heidelberg, Germany;

<sup>i</sup>Department of Physiology, University of Bern, Switzerland

# authors contributed equally

30 **\*Address for correspondence:** Patrick Lugenbiel, MD, FEHRA; Department of  
31 Cardiology, Heidelberg University, Im Neuenheimer Feld 410, 69120 Heidelberg,  
32 Germany; Tel.: ++49 6221 568855; Fax: ++49 6221 565514; E-Mail:  
33 [patrick.lugenbiel@med.uni-heidelberg.de](mailto:patrick.lugenbiel@med.uni-heidelberg.de)

#### 34 **Supplemental Methods**

35

#### 36 **Isolation of Neonatal Rat Ventricular Cardiomyocytes (NRVCs) and Cell Culture**

37 Primary cardiomyocytes were isolated from the hearts of 1- to 3-day old neonatal  
38 Wistar rats. Animal housing conditions and experimental procedures were performed  
39 in compliance with the German Law for the Protection and Use of Laboratory Animals.  
40 Rats were decapitated and the hearts dissected and washed in ice-cold Hank's  
41 balanced salt solution. Atria and large vessels were removed, ventricles were cut into  
42 small pieces and digested using DNase II (Sigma-Aldrich, St. Louis, MO) and trypsin  
43 (Thermo Fisher Scientific, Waltham, MA), performing eight 10-min digestion steps at  
44 37°C. The supernatant was collected in fetal bovine serum (FBS) after each step,  
45 pooled and centrifuged to separate the cells from remaining pieces of tissue. The cells  
46 were then resuspended in Dulbecco's modified Eagle medium (DMEM/F-12; 11039,  
47 Thermo Fisher Scientific) supplemented with 10% FBS (10270, Thermo Fisher  
48 Scientific), 1% penicillin/streptomycin (15140122, Thermo Fisher Scientific) and 1× L-  
49 glutamine (25030024, Thermo Fisher Scientific). A two-layer Percoll gradient was  
50 used to separate non-cardiomyocytes from cardiomyocytes. Collected cells were  
51 passed through a cell strainer (40µm, BD Falcon, Franklin Lakes, NJ) and then seeded  
52 into wells of 6-well cell culture plates (Thermo Fisher Scientific) coated with 0.02%  
53 gelatine (Thermo Fisher Scientific). For fluorescence recovery after photobleaching  
54 (FRAP), patch clamp and calcium transient experiments, cells were seeded on glass-



55 bottom dishes (Mattek, Ashland, OR) coated with 0.02% gelatine. The NRVCs were  
56 cultured in supplemented DMEM/F-12 as mentioned above at 37°C in 95% humidified  
57 air with 5% CO<sub>2</sub>. NRVCs showed spontaneous contraction after 24h in culture, at  
58 which time point the culture medium was replaced with fresh supplemented DMEM/F-  
59 12. NRVCs were cultured for a total of 6 days.

60

### 61 **Photon Irradiation**

62 NRVCs were subjected to 20Gy single-fraction photon irradiation on day 2 of cell  
63 culture using a biological cabinet X-ray irradiator X-RAD 320 (Precision X-Ray, North  
64 Branford, CT) at 320 keV and a dose rate of 500 cGy/min.

65

### 66 **Optical Voltage Mapping**

67 To assess the dynamics of action potential propagation in NRVC monolayers, optical  
68 mapping experiments were conducted. Using a fast and highly sensitive camera  
69 system MICAM Ultima - L (SciMedia USA, Costa Mesa, CA) and BrainVision Analyzer  
70 version 16.04.20 software (Brainvision, Tokyo, Japan), the propagation of electrical  
71 action potential in the cell cultures was recorded, visualized and analyzed. Cells were  
72 seeded in gelatin-coated 6-well plates at a density of 10<sup>6</sup> cells/well. The monolayers  
73 were incubated with 8μM of the voltage-sensitive fluorescent dye di-4-ANEPPS  
74 (D1199, Thermo Fisher Scientific) in DMEM/F-12 for 10 min in an incubator at 37°C,  
75 5% CO<sub>2</sub> and 95% humidified air. Then, fresh DMEM/F-12 medium was applied, and  
76 the cells were placed on a constant heating plate at 37°C for the duration of the  
77 experiments.

78 Action potential light ( $\lambda_{\text{ex}} = 525 \pm 25\text{nm}$ ) was emitted from a halogen arc lamp and  
79 delivered to the monolayers via epi-illumination. The fluorescent emission light ( $\lambda_{\text{em}}$   
80  $>590\text{nm}$ ) was first passed through a diverging lens (1× Plan-Apo, WD=61.5mm; Leica,  
81 Wetzlar, Germany) and then a dichroic mirror and eventually focused on a 100×100  
82 pixels complementary metal oxide semiconductor camera (MiCAM05-Ultima,  
83 SciMedia) through a 2× converging lens. The cells were electrically stimulated for the  
84 experiments at a frequency of 1Hz with an epoxy resin-coated bipolar platinum  
85 electrode (pulse strength 8V, pulse duration 10ms). The electrode was connected to  
86 a stimulus generator STG 2004 (Multi Channel Systems, Reutlingen, Germany)  
87 controlled by the software MC Stimulus II (v3.5.0, Multi-Channel Systems). The signals  
88 were acquired at a spatial resolution of 205  $\mu\text{m}/\text{pixel}$ . The velocity of propagation and  
89 action potential characteristics were recorded during electrical stimulation at 1Hz.  
90 Signals were averaged with those from the 8 nearest pixels to minimize noise  
91 artefacts. The conduction velocity was analyzed, and action potential duration (APD)  
92 was calculated at 50% (APD<sub>50</sub>) and 90% (APD<sub>90</sub>) of repolarization. Statistical analysis  
93 was performed using GraphPad Prism 6 software (GraphPad Software, San Diego,  
94 CA).

### 95 **Video Analysis of Beat Frequency**

96 Beat frequency in recorded videos of cardiomyocytes was measured using the  
97 recently developed macro Myocyter (version 1.0), an analytical software tool for the  
98 ImageJ (version 1.52b) image processing software.<sup>1</sup> By scaling the time-dependent  
99 changes in pixel intensity in successive video images of recorded cardiomyocytes,  
100 Myocyter allowed visualization of cellular contractility. Spontaneous contractions of  
101 neonatal cardiomyocytes were recorded using an iPhone XR (Apple, Cupertino, CA)

102 connected to the eyepiece of a Leica DMI1 microscope via a camera adapter (Bresser,  
103 Rhede, Germany). Video recordings were done at 60 frames/s for 10-15s. Data  
104 extraction with Myocyter was performed according to the developer's instructions and  
105 beat frequency was analyzed using ImageJ 1.50i.<sup>2</sup>

106

### 107 **RNA Isolation and Reverse Transcription Quantitative Real-Time PCR (RT- 108 qPCR)**

109 RNA isolation and RT-qPCR were performed as published elsewhere.<sup>3</sup> Briefly, RNA  
110 was isolated using QIAzol Lysis Reagent (Qiagen, Hilden, Germany) according to the  
111 manufacturer's instructions. RNA concentration was determined using a NanoDrop  
112 2000/2000c spectrophotometer (Thermo Fisher Scientific) at a wavelength of  $\lambda=260$   
113 nm. The isolated RNA (3 $\mu$ g) was converted into DNA using the Maxima First Strand  
114 cDNA Synthesis Kit for RT-qPCR (Thermo Fisher Scientific) according to the  
115 manufacturer's instructions. RT-qPCR was performed using the StepOnePlus PCR  
116 System (Thermo Fisher Scientific) and TaqMan Gene Expression Assay primers  
117 (Applied Biosystems, Foster City, CA; see Supplemental Table 1). Normalization was  
118 done using primers and probes for the housekeeping enzyme glyceraldehyde-3-  
119 phosphate dehydrogenase (GAPDH) using delta-delta-Ct method. All RT-qPCR  
120 reactions were performed in triplicate or a higher number of replicates, and a non-  
121 template control and dilution series were included on each plate for quantification.  
122 Data are expressed as the average of triplicates. All measurements were adjusted  
123 using a standard probe, and quantification was corrected for the amplification  
124 efficiency derived from the standard curves.

125

**126 Protein Isolation and Western Blot Analysis**

127 Proteins were extracted from NRVC and protein immunodetection was performed by  
128 sodium dodecyl sulfate (SDS)-polyacrylamide (PAA) gel electrophoresis and western  
129 blotting as previously reported.<sup>3</sup> Proteins were extracted in 20mM Tris-HCl, 0.5%  
130 Nonidet P-40, 0.5% sodium deoxycholate, 150mM NaCl, 1 mM EDTA, 1mM Na<sub>3</sub>VO<sub>4</sub>,  
131 1mM NaF and inhibitors of proteases (cOmplete, Mini Protease Inhibitor Cocktail;  
132 Roche Applied Science, Indianapolis, IN). The resulting samples were centrifuged at  
133 4°C for 30 min and 14,000×g, and the protein concentration in the supernatants was  
134 determined by the bicinchoninic acid protein assay (Thermo Fisher Scientific). Equal  
135 amounts of total protein were separated on SDS- 7.5-15% PAA gels and transferred  
136 to nitrocellulose membranes for 2h at 200mV (Amersham Protran 0.45 NC; GE  
137 Healthcare Life Sciences, Freiburg, Germany). After blocking in PBST containing 5%  
138 non-fat milk for 2h at room temperature (RT), membranes were incubated overnight  
139 with the primary antibodies listed in Supplemental Table 2. Next, the membranes were  
140 incubated with matching horseradish peroxidase (HRP)-conjugated goat anti-rabbit  
141 secondary antibody (ab6802, Abcam, Cambridge, United Kingdom), HRP- conjugated  
142 goat anti-mouse IgG (H+L) secondary antibody (1031-05, Southern Biotech,  
143 Birmingham, AL) or HRP-conjugated goat anti-mouse IgG1 cross-adsorbed  
144 secondary antibody (A10551, Thermo Fisher Scientific,). Signals were developed with  
145 the enhanced chemiluminescence detection reagent (ECL Western blotting Reagents;  
146 GE Healthcare, Buckinghamshire, United Kingdom). GAPDH was used as an internal  
147 control. Quantification of optical density was performed with ImageJ 1.50i software.

148

149

**150 FRAP**

151 FRAP was assessed as an indicator of gap junctional coupling efficiency.  
152 Photobleaching and imaging were performed on an Olympus FluoView confocal laser  
153 scanning microscopy (Olympus Corporation, Tokyo, Japan) using a 60x water  
154 immersion objective (1.2 NA). NRVC monolayers seeded on glass-bottom dishes were  
155 incubated for 20 min in the dark with 500 $\mu$ l of 0.5 $\mu$ M calcein-AM (Thermo Fisher  
156 Scientific) in Tyrode's solution. Calcein-AM was converted to green fluorescent calcein  
157 by intracellular esterases. After de-esterification, cells were washed with prewarmed  
158 Tyrode's solution for 10 min. Afterwards, the dye was no longer able to diffuse through  
159 the plasma membrane and could only leave cells through gap junctions. One  
160 cardiomyocyte within a monolayer was bleached with a laser power of 50% at 10  
161  $\mu$ s/pixel for 5s. Calcein diffusion from neighbouring cells into the bleached cell was  
162 measured over time and recovery of fluorescence was recorded in 50 images taken  
163 every 10s with a laser power of 0.5% at 2 $\mu$ s/pixel. Analysis was done in ImageJ to plot  
164 the time course of fluorescence recovery. After subtraction of background  
165 fluorescence and bleaching area, the plot was normalized to the fluorescence intensity  
166 before bleaching. Parameters were analysed using OriginLab software (OriginLab  
167 Corporation, Northampton, MA) and ImageJ 1.50i software.

**168 Immunofluorescence Analysis**

169 NRVCs on 20x20mm glass coverslips were washed with cold phosphate-buffered  
170 saline (PBS) for three times, fixed with 4% paraformaldehyde solution in PBS (Roti-  
171 Histofix, Carl Roth, Karlsruhe, Germany) for 10 min at RT. Cells were permeabilized  
172 with PBS containing 0.1% Triton X-100 (Merck, Darmstadt, Germany) for 3 min,  
173 followed by a blocking step with 5% Gibco normal goat serum (Thermo Fisher

174 Scientific) and 0.1% Triton X-100 in PBS for 2h. Cells were incubated overnight with  
175 the following primary antibodies: rabbit polyclonal to connexin 43 (Cx43), mouse  
176 monoclonal to cardiac troponin T (cTnT), rabbit polyclonal to cTnT and mouse  
177 monoclonal to vimentin. Next, cells were incubated with matching secondary  
178 antibodies conjugated to Alexa Fluor dyes with different excitation-emission spectra  
179 for 2h at RT and protected from light, using Alexa Fluor 568-conjugated donkey-anti-  
180 rabbit IgG (H+L) (A11057, diluted 1:1000; Thermo Fisher Scientific) or Alexa Fluor  
181 488-conjugated goat-anti-mouse IgG (H+L) (A32723; diluted 1:1000, Thermo Fisher  
182 Scientific). All antibodies were diluted in blocking buffer. Cells were mounted with  
183 Fluoroshield (Sigma-Aldrich containing DAPI (4',6-diamidino-2-phenylindol  
184 dihydrochloride (Abcam) for nuclear staining. Laser-scanning confocal imaging was  
185 used to estimate the expression of Cx43. Images were taken on a Leica SP8 confocal  
186 microscope with a 63x oil immersion objective and analyzed using the ImageJ 1.50i  
187 software. All immunofluorescence images were taken at the same light intensity and  
188 photodetector setting to ensure a fair comparison. Cell surface Cx43 levels were  
189 expressed as the ratio of the area of Cx43 plaque to the intercellular border area.

### 190 **Calcium Transient Measurements**

191 Calcium transients of NRVCs were measured with the calcium- sensitive fluorescent  
192 dye fura-2-AM (Thermo Fisher Scientific). NRVCs seeded on glass-bottom dishes  
193 were loaded with 1.5 $\mu$ M of fura-2-AM in Tyrode's solution and incubated for 20 min,  
194 followed by washing with Tyrode's solution and waiting 10 min for de-esterification.  
195 Cells were continuously perfused with pre-heated Tyrode's solution containing  
196 Probenecid (100 $\mu$ M; Sigma Aldrich) to prevent secretion of fura-2. Calcium transients  
197 were recorded using an IonOptix system (IonOptix, Dublin, Ireland). NRVCs were

198 exposed to light from a xenon lamp passing through fast-switching filters of 340nm  
199 and 380nm to determine the ratio of bound and unbound calcium ions in the cells.  
200 Fluorescence emission light was collected at 510nm. Data are presented as fura-2  
201 ratio (F340/F380nm) and collected using the IonWizard software developed by  
202 IonOptix. Three representative calcium transients were analysed per recording using  
203 OriginPro software. Assessed parameters comprised diastolic calcium level,  
204 amplitude, time-to-peak, full duration at half maximum and decay. Decay of calcium  
205 transients was calculated using an exponential decay function.

206

#### 207 **Terminal Deoxynucleotidyl Transferase dUTP Nick End Labeling (TUNEL)** 208 **Staining**

209 TUNEL staining was performed using the In Situ Cell Death Detection Kit, TMR red of  
210 Roche Applied Science according to the manufacturer's protocol. Cells on glass  
211 coverslips were washed three times with PBS and then fixed with 4% buffered  
212 paraformaldehyde for 10 min. After another washing step, the cells were  
213 permeabilized by incubation with 0.1% Triton- X100 in PBS for 2 min at 4°C. The  
214 positive control consisted of permeabilized cells treated for 10 min at RT with  
215 recombinant DNase I (3U/ml in 50 mM Tris-HCl (pH 7.5); Roche, Mannheim,  
216 Germany), 1mg/ml bovine serum albumin) to induce double-strand breaks. Next, 5 $\mu$ l  
217 Enzyme Solution and 45 $\mu$ l Label Solution were mixed and added to each coverslip.  
218 Instead of the reaction mix, 50 $\mu$ l Label Solution was added to the negative control  
219 sample. After incubation for 1h in a humidified dark chamber at 37°C, the coverslips  
220 were washing three times with PBS covered with antifade containing For  
221 immunofluorescent stainings evaluating the proportion of cardiomyocytes and

222 fibroblasts in culture, imaging was performed with an inverted Axio Observer Z1  
223 microscope and an Axiocam 506 camera (Carl Zeiss) Cells were labelled with rabbit  
224 polyclonal anti-troponin T antibodies to identify (cardiomyocytes and mouse  
225 monoclonal anti-vimentin antibodies to mark cardiac fibroblasts. Secondary antibodies  
226 were Alexa Fluor 568-conjugated donkey-anti-rabbit (A11057, diluted 1:1000; Thermo  
227 Fisher Scientific) and Alexa Fluor 488-conjugated goat-anti-mouse (A32723; diluted  
228 1:1000, Thermo Fisher).

229 Immunofluorescence analysis of cell culture was performed with an inverted Axio  
230 Observer Z1 microscope (Carl Zeiss, Jena, Germany) and an Axiocam 506 camera  
231 (Carl Zeiss). TUNEL-positive cells were counted manually, and ImageJ 1.41 software  
232 was used to calculate the total cell number in 3x3 tiles. Excitation wavelengths in the  
233 range of 520-560nm (maximum 540nm; green) were used as well as detection  
234 wavelengths in the range of 570-620nm (maximum 580nm, red). The percentage of  
235 TUNEL-positive cells was calculated by dividing TUNEL-positive cells by total cell  
236 count.

### 237 **Patch Clamp Recordings of Action Potentials**

238 For action potential recordings, NRVCs were cultured on 35mm glass-bottom dishes  
239 at single cell density. Measurements were performed in whole-cell patch-clamp  
240 configuration using a HEKA EPC-10 patch clamp amplifier (HEKA Instruments,  
241 Holliston, MA) connected to an inverted Olympus IX81 FluoView1000confocal laser  
242 scanning microscope (Olympus, Tokyo, Japan) as previously described.<sup>2</sup> Data were  
243 acquired using PatchMaster (HEKA Instruments). Glass pipettes were pulled from  
244 borosilicate glass capillaries (GB150-8P; Science Products Hofheim am Taunus,  
245 Germany) using a DMZ Universal Puller (Zeitz Instruments, Martinsried, Germany) to



246 achieve pipette resistances of 1.5 - 2.5M $\Omega$ . The intracellular solution consisted of 120  
247 mM KCl, 10mM HEPES, 5mM MgCl<sub>2</sub>, 5 mM EGTA, 2.5mM Na<sub>2</sub>-ATP, and the pH was  
248 adjusted to 7.2 using KOH. The external solution contained normal Tyrode (140mM  
249 NaCl, 6mM KCl, 1.8mM CaCl<sub>2</sub>, 1.1mM MgCl<sub>2</sub>, 10mM D-glucose, 10mM HEPES) and  
250 the pH was adjusted to 7.4 using NaOH. To determine the action potential stimulation  
251 threshold, a series of stepwise increasing stimulation currents (ranging from 100pA to  
252 500nA with a step size of 100pA) was delivered. The first current resulting in an  
253 amplitude above the threshold was used to trigger action potentials. Action potential  
254 parameters were analyzed using OriginPro software.

255

256

257

258

259

260

261

262

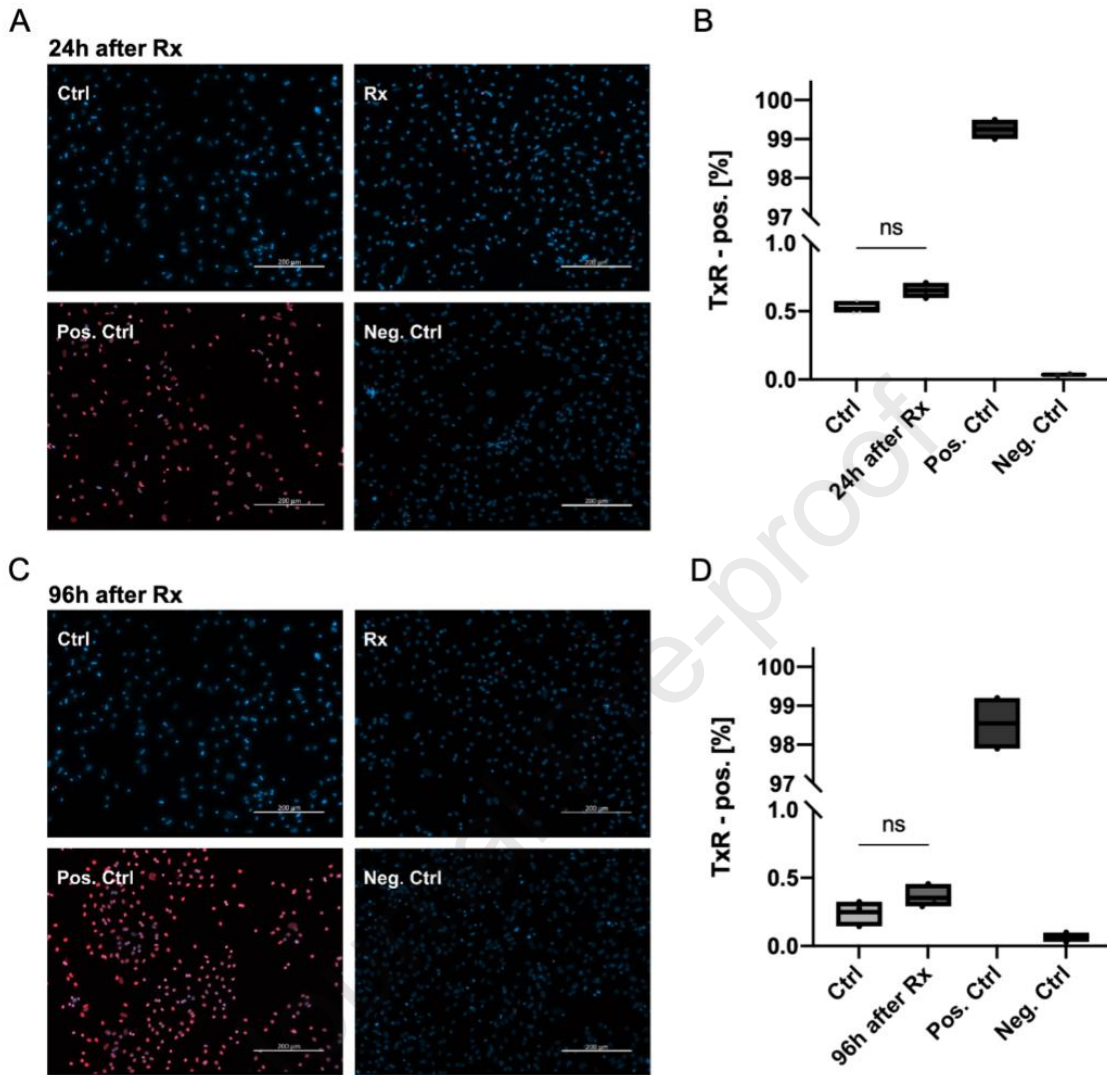
263

264

265

266

267

268 **Supplemental Figures and tables**

269

270 **Supplemental Figure 1: Irradiation did not impact apoptosis rate in NRVCs.**

271 Representative fluorescence stainings of TUNEL assays (scale bar, 100 $\mu$ m) at (A) 24h

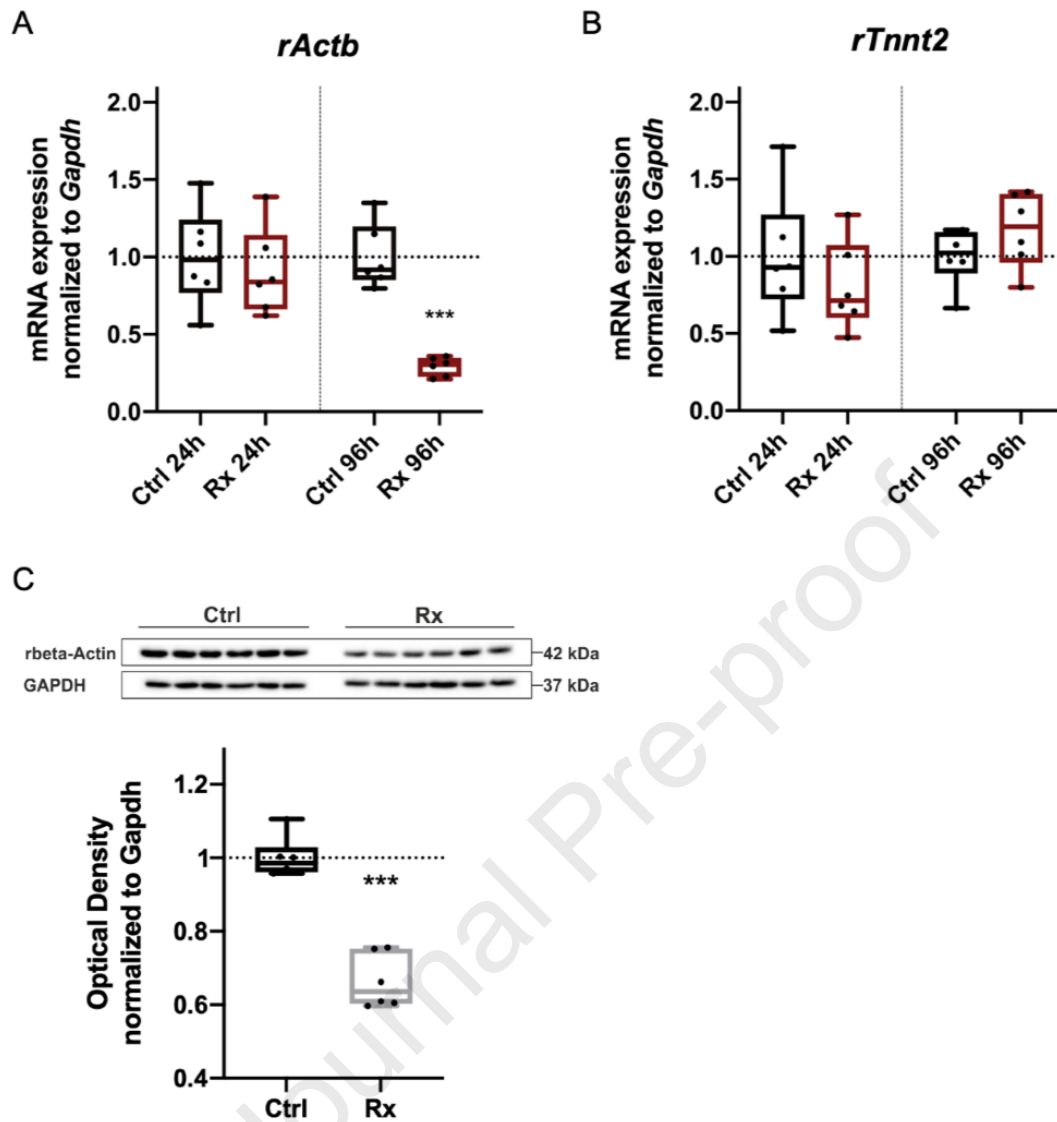
272 and (C) 96h after radiation (Rx). Red nuclear fluorescence reflects endonucleolytic

273 DNA degradation and apoptosis. Mean apoptosis rates at (B) 24h ( $n=3$ , each) and (D)

274 96h after Rx ( $n=3$ , each). TUNEL (Texas Red, TxR)-positive cells are expressed in

275 relation to the total number of cells. Data are shown as box and whisker plots. Ctrl,

276 control.

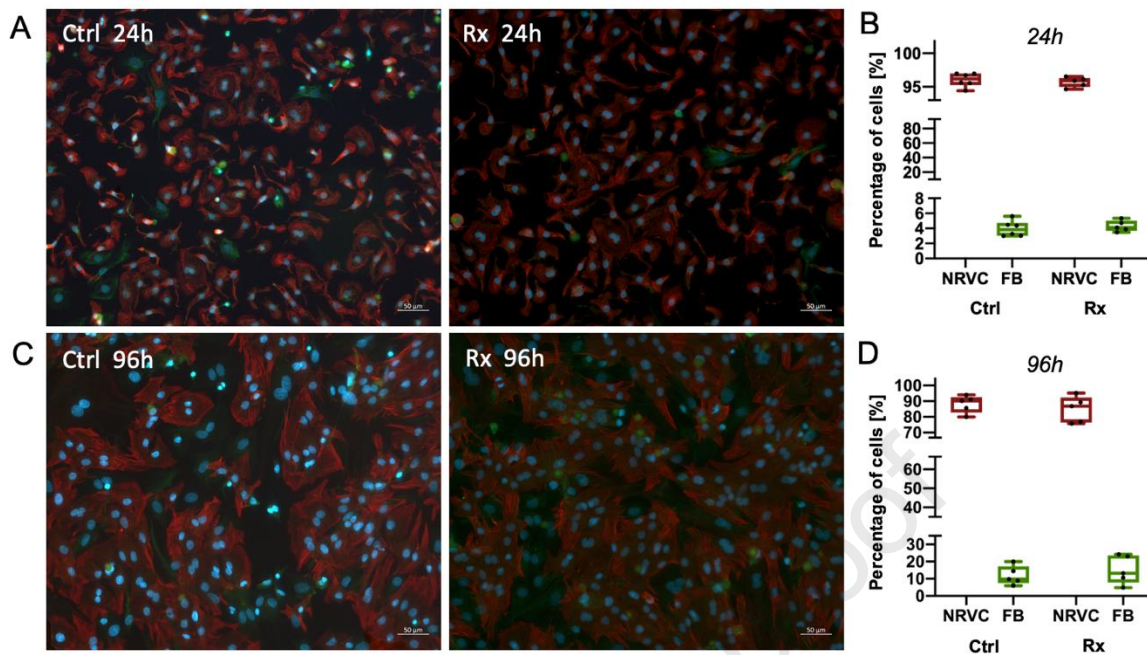


277

278 **Supplemental Figure 2: Structural changes after irradiation.** RT-qPCR analysis of279 (A) *Actb* mRNA ( $n=6$ , each). and (B) *Tnnt2* mRNA ( $n=6$ , each) levels in irradiated (Rx)

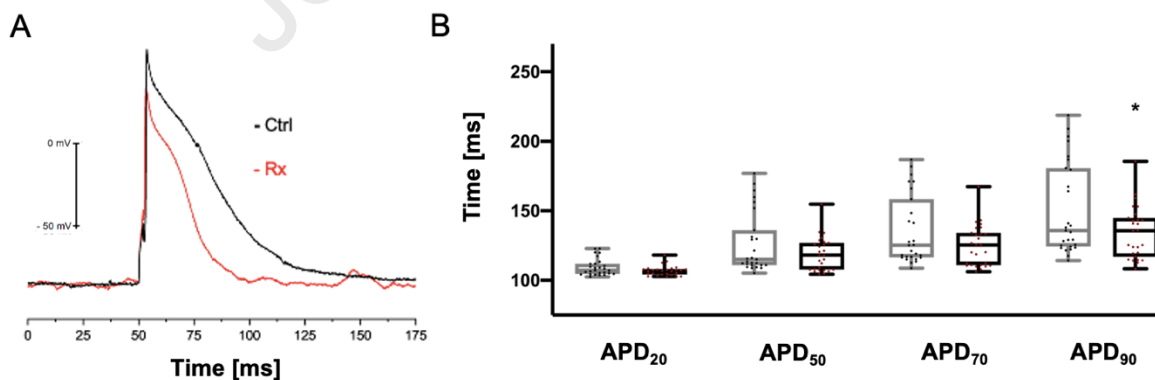
280 and non-irradiated (Ctrl) NRVCs. (C) Western blot analysis of beta-actin protein levels

281 ( $n=6$ , each) in irradiated and Ctrl NRVCs. Data are shown as box and whisker plots.282 (\* $p<0.05$ , \*\* $p<0.01$ , \*\*\* $p<0.001$ ).



283

284 **Supplemental Figure 3: NRVC to cardiac fibroblast ratio at 24h and 96h after**  
 285 **irradiation.** Representative stainings of cardiomyocytes (red, cTNT) and fibroblasts  
 286 (green, vimentin) (A) 24h and (C) 96h after irradiation (Rx). Analysis of the ratio of  
 287 cells in culture (B) 24h after Rx (Ctrl:  $n=5$ , Rx:  $n=6$ ) and (D) 96h after Rx ( $n=5$ , each).  
 288 Data are shown as box and whisker plots. Ctrl, control.



289

290 **Supplemental Figure 4: Action potential characteristics of control and irradiated**  
 291 **cardiomyocytes 24h after Rx.** (A): Representative traces of ventricular action  
 292 potentials of control cardiomyocytes (black) and irradiated cardiomyocytes (red) at 24h

293 after Rx. (B): Analysis of resting membrane potential (RMP), action potential amplitude  
 294 (APA) and action potential duration at 20%, 50%, 70% and 90% repolarization (APD<sub>20</sub>,  
 295 APD<sub>50</sub>, APD<sub>70</sub>, APD<sub>90</sub>),  $n=27$ , each. Data are shown as box and whisker plots.  
 296 (\* $p<0.05$ ).

297

298 **Supplemental Table 1:** PCR primers sorted alphabetically

<b>Primer</b>	<b>ThermoFisher Catalogue Number</b>	<b>Chromosome Location</b>
rActb	Rn00667869_m 1	Chr.12: 13715843 - 13718813 on Build Rnor_6.0
rAtp2a1	Rn01508014_m 1	Chr.1: 197855912 - 197875038 on Build Rnor_6.0
rCacna1c	Rn00709287_m 1	Chr.4: 150639043 - 151269159 on Build Rnor_6.0
rCamklIδ	Rn00560913_m 1	Chr.2: 230900907 - 231130336 on Build Rnor_6.0
rCamklIγ	Rn01537033_m 1	Chr.15: 3936714 - 3995740 on Build Rnor_6.0
rGapdh	Rn01775763_g1	Chr.4: 157676396 - 157680271 on Build Rnor_6.0
rGja1	Rn06415115_s1	Chr.20: 37876589 - 37889097 on Build Rnor_6.0

rKcnd3	Rn04339184_m 1	Chr.2: 207923775 - 208140727 on Build Rnor_6.0
rKcne1	Rn01767120_m 1	Chr.11: 32498260 - 32508420 on Build Rnor_6.0
rKcnh2	Rn01442522_m 1	Chr.4: 7355161 - 7387243 on Build Rnor_6.0
rKcnj12	Rn02533449_s1	Chr.10: 47282208 - 47343501 on Build Rnor_6.0
rKcnj2	Rn00568808_s1	Chr.10: 99429265 - 99442520 on Build Rnor_6.0
rKcnj8	Rn01492857_m 1	Chr.4: 176783287 - 176789143 on Build Rnor_6.0
rKcnk2	Rn00597042_m 1	Chr.13: 107690111 - 107886476 on Build Rnor_6.0
rKcnk3	Rn04223042_m 1	Chr.6: 27154274 - 27190209 on Build Rnor_6.0
rKcnq1	Rn00583376_m 1	Chr.1: 216293087 - 216630339 on Build Rnor_6.0
rPln	Rn01434045_m 1	Chr.20: 34633157 - 34642904 on Build Rnor_6.0
rRyr2	Rn01470303_m 1	Chr.17: 65533998 - 65955606 on Build Rnor_6.0
rScn5a	Rn00565502_m 1	Chr.8: 128169191 - 128266639 on Build Rnor_6.0

rSlc8a1	Rn04338914_m 1	Chr.6: 4245582 - 4564263 on Build Rnor_6.0
rTnnt2	Rn00562059_m 1	Chr.13: 52662973 - 52680992 on Build Rnor_6.0

299

300 **Supplemental Table 2:** Western blotting antibodies sorted alphabetically.

Primary Antibody	Class	Host	Dilution	Company
Anti-alpha-smooth-muscle-actin (14-9760-82)	monoclonal	mouse	1:1000	Invitrogen, Thermo Fisher Scientific
Anti-beta actin antibody (ab8227)	polyclonal	rabbit	1:3000	Abcam
Anti-CaMKII delta antibody (ab181052)	polyclonal	rabbit	1:1000	Abcam
Anti-CaMKII gamma antibody (ab262701)	polyclonal	rabbit	1:1000	Abcam
Anti-Cav1.2 (CACNA1C) antibody (MA5-27717)	monoclonal	mouse	1:1000	Invitrogen, Thermo Fisher Scientific
Anti-Cx43 antibody (ab11370)	polyclonal	rabbit	1:3000	Abcam
Anti-GAPDH antibody (ab181602)	polyclonal	rabbit	1:10000	Abcam

Anti-KCNK2/TREK-1 antibody (APC-047)	polyclonal	rabbit	1:1000	Abcam
Anti-Kir2.1 (KCNJ2) antibody (APC-026)	polyclonal	rabbit	1:1000	Abcam
Anti-Kir6.1 (KCNJ8) antibody (ab241996)	monoclonal	mouse	1:1000	Abcam
Anti-Kv11.1 (KCNH2) antibody (APC-062)	polyclonal	rabbit	1:1000	Abcam
Anti-Kv4.3 (KCND3) antibody (APC-017)	polyclonal	rabbit	1:1000	Abcam
Anti-Kv7.1 (KCNQ1) antibody (MA5-27676)	monoclonal	mouse	1:1000	Invitrogen, Thermo Fisher Scientific
Anti-Nav1.5 (SCN5A) (493-511) antibody (ASC-005)	polyclonal	rabbit	1:500	Alomone Labs
Anti-NCX (SLC8A1) antibody (ASC-005)	polyclonal	rabbit	1:1000	Alomone Labs
Anti-Phospholamban (PLN) (MA3-922)	monoclonal	mouse	1:1000	Invitrogen, Thermo Fisher Scientific
Anti- Vimentin (VIM) antibody (ab8069)	monoclonal	mouse	1:1000	Abcam

301

302



303 **Supplemental references**

- 304 1. Rasband, W.S., ImageJ, U. S. National Institutes of Health, Bethesda, MA,  
305 <https://imagej.net/ij/>, 1997-2018.
- 306 2. Grune T, Ott C, Häseli S, Höhn A, Jung T. The “MYOCYTER” – Convert cellular  
307 and cardiac contractions into numbers with ImageJ. Sci Rep. 2019;9:15112.
- 308 3. Syren P, Rahm A-K, Schweizer PA, et al. Histone deacetylase 2-dependent  
309 ventricular electrical remodeling in a porcine model of early heart failure. Life Sci.  
310 2021;281:119769.